Exciton Modeling of Energy-Transfer Dynamics in the LHCII Complex of Higher Plants: A Redfield Theory Approach

Vladimir Novoderezhkin,[†] **Jante M. Salverda,**[‡] **Herbert van Amerongen,**[‡] **and Rienk van Grondelle*,**[‡]

A. N. Belozersky Institute of Physico-Chemical Biology, Moscow State University, Leninskie Gory, 119992, Moscow, Russia, and Department of Biophysics, Faculty of Sciences, Vrije Universiteit, De Boelelaan 1081, 1081 HV Amsterdam, The Netherlands

We propose an exciton model for the peripheral plant light-harvesting complex LHCII that allows us to explain the absorption (OD) and linear dichroism (LD) spectra, the superradiance (SR), the pump−probe transient absorption (TA), the three-pulse photon echo peak shift (3PEPS), and transient grating (TG) kinetics at different excitation wavelengths. To calculate the nonlinear response we used the Liouville equation for the density matrix, expanded up to the third order with respect to the external field, with the Redfield relaxation superoperator in the exciton eigenstate basis. We found a few configurations of the antenna, with specific chlorophyll (Chl) *a/b* identities, orientations, and site energies, that allowed a simultaneous fit of these data while taking into account the excitonic interactions, the static disorder, and weak exciton−phonon coupling which induced dephasing and relaxation (energy transfer) between the exciton states. The spectral density of the exciton−phonon coupling adjusted from the fit allowed us to determine the time scales and pathways of energy transfer in LHCII. We find that the intraband (Chl *b*→Chl *b* and Chl *a*→Chl *a*) energy-transfer dynamics includes sub-picosecond (250−600 fs) exciton relaxation within dimeric or, in the Chl *a* band, more complicated clusters, sub-picosecond (600−800 fs) hopping between spatially separated clusters (in the *a* band), and "slow" (picosecond) migration between localized states. The interband (Chl *b*→Chl *a*) transfer is characterized by the presence of very fast channels, the fastest taking only 120 fs, which connect both localized and dimeric *b* states with the *a* band. The overall relaxation/migration dynamics can be directly viewed by means of the time-dependent density matrix in the exciton and site representation. The latter representation allows us to visualize the time-dependent degree of delocalization. While the individual exciton states can be delocalized over 2−2.5 molecules in the Chl *a* region, thermal mixing results in a coherence size of 1.4−1.8 for the steady-state wave packet at room temperature. Altogether, we conclude that the experimentally determined dynamic and static properties of LHCII can be simulated very well on the basis of the proposed excitonic model.

Introduction

Following the absorption of solar photons by photosynthetic pigments, the excited state energy is rapidly and efficiently transferred to the reaction center, where a charge separation is initiated.[1] During the past decade, the study of the energy-transfer dynamics taking place in the peripheral light-harvesting complexes from higher plants has attracted much effort (see ref 2 for a review) following the discovery of the crystal structure of the major antenna complex LHCII.[3] The LHCII structure was modeled with 3.4 Å resolution, which did not allow for a distinction between chlorophyll (Chl) *a* and *b* or between *X*- and *Y*-axes of the Chls. Thus, the identities of the Chls at the twelve discernible binding sites and the direction of their dipole moments were assigned in a hypothetical fashion. The interpretation of the highly inhomogeneous spectra and of the multicomponent energy transfer kinetics in LHCII still remains a very complicated and puzzling problem.

Several site-directed mutagenesis studies of the chlorophyll binding residues have been carried out to determine the Chl identities in LHCII[4−7] and the similar complex CP29.[8,9] Remelli et al.[4] concluded that the sites A_1, A_2, A_4, A_5, and B_1 are occupied by Chls *a*, and the sites B_2, B_5, and B_6 by Chls *b*, whereas A_3, A_6, A_7, and B_3 are "mixed" sites which can bind both Chls *a* and Chls *b*. This result was contested by Rogl and co-workers[5,7] who assume that mixed binding sites cannot occur in native complexes and find that the A_3 and B_3 sites both bind Chls *a*. In a more recent assignment of Bassi [private communication] a Chl *b* is proposed to bind at site A_7 whereas the other three sites remain mixed. Using the identities proposed by Remelli et al., İşeri and Gülen[10] attempted to assign the orientations of the Chls by modeling the absorption (optical density, OD) and linear dichroism (LD) spectra of LHCII. They supposed that all mixed sites have equal probability to bind Chl *a* or *b*, thus considering all 16 possible configurations of $A_3A_6A_7B_3$ from *aaaa* to *bbbb*. A satisfactory fit of the OD and LD spectra was obtained for the orientations $A_1A_2A_3A_4A_5A_6A_7$ $B_1B_2B_3B_5B_6 = 0100000\ 00110$, with the notations "0" meaning along the N_A−N_C axis and "1" along N_B−N_D, as proposed by Gülen.[11] To obtain a good fit for the LD spectrum in the Chl *b*

* To whom correspondence should be addressed. E-mail: rienk@nat.vu.nl. Fax: +31-20-4447899.
† Moscow State University.
‡ Vrije Universiteit.

region, İşeri and Gülen also introduced some additional rotations of the Chl *b* dipole moments. It should be realized that the dipole orientations may well be different from the ones given by Kühlbrandt, so that LD spectrum calculations based on it remain an approximation. To calculate these spectra, they used standard exciton theory without taking into account any spectral disorder and realistic line shapes. However, the site inhomogeneity value for LHCII is about $120-140$ cm^{-1} (see discussion in the review of van Amerongen and van Grondelle, ref 2), which is comparable with the strongest excitonic couplings in the complex. Such disorder will mix the zeroth-order wave functions, producing a new exciton structure of the complex. Subsequently, the delocalization features and the dynamics of the excitation relaxation/hopping will be significantly affected. A more sophisticated exciton theory, including static disorder and exciton-vibrational coupling, was developed by Renger and May[12] in order to explain the temperature dependence of the OD spectra of LHCII.

The excitonic interactions in the Chl *a* band of LHCII were studied by a combination of nonlinear absorption and nonlinear polarization techniques.[13] The data revealed one spectral form with a dipole strength of 2.3 (in units of monomeric dipole strength). On the other hand, the superradiance data[14] have shown that the total (thermally averaged) emitting dipole strength of the antenna is within the range of $1-1.2$.

The dynamical behavior of LHCII, specifically the energy transfer between the chlorophylls, was studied with various time-resolved nonlinear spectroscopic methods. Pump−probe and fluorescence studies revealed that Chl *b* to Chl *a* transfer takes place with two major time constants of ∼300 and ∼600 fs at 77K,[15−19] or ∼150 and ∼600 fs at room temperature[15,20−22] and a minor $4-9$ ps component. Equilibration within the Chl *a* manifold occurs to a large extent within a few hundred fs, but upon blue side excitation slow ps components are also observed.[16,18] Three-pulse photon echo peak shift (3PEPS) measurements on LHCII at room temperature have been performed recently using 650 and 670 nm excitation, corresponding to the Chl *b* and *a* regions, respectively.[23,24] Where the pump−probe technique mainly monitors downhill ("interband") energy transfer, the three-pulse photon echo technique is more sensitive to the intraband Chl *a*−Chl *a* and Chl *b*−Chl *b* transfer processes.[25] Agarwal et al.[23] analyzed their data using a theory that includes a simple energy transfer model,[25] based on hopping of localized excitations with phenomenological rate constants as free parameters. They also incorporated exciton−phonon coupling by convoluting the energy transfer function with a single-site correlation function, which consists of a sum of Gaussian, exponential and damped cosine contributions. Their modeling showed sub-picosecond Chl *b*−Chl *b* transfer for the first time. They also identify contributions from the well-known Chl *b*→Chl *a* transfer processes, which take place in 150 fs, 600 fs, and 4 ps, and from Chl *a*−Chl *a* equilibration occurring on time scales from 300 fs to 6 ps.

In this paper we propose a new model for the LHCII antenna which includes pigment identities, dipole moment orientations and unperturbed site energies. We calculate several LHCII properties using an exciton theory which includes spectral disorder. The homogeneous broadening of the exciton components is determined in the weak exciton−phonon coupling limit using Redfield relaxation theory.[26] The model allows us to explain the linear OD and LD spectra. Furthermore, the Redfield theory provides us with the relaxation parameters needed to calculate the excitation dynamics in the exciton eigenstate basis. Such an approach was used to study the dynamics within a Chl

b−Chl *a* heterodimer of LHCII.[27] We are the first to apply this method to the whole LHCII antenna, for which the dynamic properties have so far always been calculated using Förster theory.[28] Thus we have a unified physical approach making it possible to model simultaneously the linear spectra and the dynamics of the nonlinear spectral response. We aim to obtain a self-consistent fit of the OD and LD spectra, the superradiance (SR), the pump−probe transient absorption (TA) kinetics, the three-pulse photon echo peak shift (3PEPS), and transient grating (TG) kinetics. We find a few configurations of the antenna that allow us to obtain a simultaneous fit of all these data. For these configurations, we can calculate the time scales and pathways of energy transfer, and directly visualize these events using the time-dependent density matrix.

The Model

We consider a monomeric LHCII complex consisting of 12 chlorophyll (Chl) molecules at sites A_1, A_2, A_3, A_4, A_5, A_6, A_7, B_1, B_2, B_3, B_5, and B_6 (nomenclature from Kühlbrandt et al.[3]), where sites A_1, A_2, A_4, A_5, and B_1 bind Chls *a*, sites B_2, B_5, and B_6 bind Chls *b*, sites A_3 and B_3 each bind on average 0.5 Chl *a* and 0.5 Chl *b*, and sites A_6 and A_7 together bind 0.5 Chl *a* and 1.5 Chl *b* (based on Remelli et al., ref 4). This means that one LHCII subunit contains on average 6.5 Chls *a* and 5.5 Chls *b*. We checked out all possible realizations of pigment identities at mixed sites with 7 Chls *a* and 5 Chls *b* per subunit (combinations $A_3A_6A_7B_3 = abab$, *abba*, *baab*, *baba*, *aabb*, and *bbaa*), as well as the realizations with 6 Chls *a* and 6 Chls *b* per subunit which have two Chls *b* on A_6-A_7 (combinations $A_3A_6A_7B_3 = abbb$, *bbba*). For each of these eight configurations, we tried to obtain a simultaneous fit of the OD, LD, SR, TA, TG, and 3PEPS data using different orientations and site energies of the chlorophylls. To calculate the linear and nonlinear spectral response we used the Redfield relaxation theory, which is based on the assumption of weak coupling of the electronic excitations to phonons. In this approach the spectral density of the exciton−phonon coupling determines the line broadening as well as the relaxation parameters.[26,29−35] The simultaneous fit of many static and dynamic properties will allow us to fix the parameters of static and dynamic disorder that determine all the relaxation rates for populations and coherences in the one-exciton manifold of the LHCII antenna. Thus, the time scales and pathways of the energy-transfer dynamics, which includes dynamic localization and noncoherent migration of the excitation, can be directly followed through the evolution of the time-dependent density matrix in the exciton and site representation.

The exciton Hamiltonian was calculated in the dipole−dipole approximation. Starting out from the site representation, diagonal elements of the Hamiltonian are given by the unperturbed site energies of the Chls. Off-diagonal elements are given by the dipole−dipole approximation of the interaction between the Chls at the sites concerned. The diagonalization of the system Hamiltonian allows the calculation of the linear and nonlinear spectral response in the eigenstate basis by using the density matrix equation with the Redfield relaxation tensor. The theory of the photon echo signal calculation is given in Appendix A, whereas the pump−probe simulation using the Redfield formalism is described elsewhere.[30,34]

In our modeling, the S_0-S_1 transition energies of the sites are varied until the best fit is obtained. The energy of the S_1-S_2 transition was supposed to be 100 cm^{-1} blue-shifted with respect to that of the S_0-S_1 transition.[36] According to ref 2 the effective dipole strength f^2d^2/ϵ (where f is the local field

LHCII Complex of Higher Plants

J. Phys. Chem. B, Vol. 107, No. 8, 2003 **1895**

correction factor and ϵ is the relative dielectric constant) is taken to be 17.6 D^2 for the S_0–S_1 transition in Chl a (assuming a value of $n = 1.54$ and the dipole–refraction index relation as described by Knox[37]). The dipole moment d was reduced by 0.84 for the S_0–S_1 transition in Chl b^2 and by 0.9 (or 0.9·0.84) for the S_1–S_2 transitions in Chl a (or b).[36]

The elements of the Redfield relaxation tensor defined by eqs A10 and A11 describe the connection between exciton levels. For example, the population transfer between one-exciton states k and k' is given by the term $\sum_{nmn'm'} c_{nk} c_{mk} c_{n'k'} c_{m'k'} J_{k'k} \langle v_{nm} v_{n'm'} \rangle$, where c_{nk} is the wave function amplitude of the n-th molecule participating in the kth exciton state, $J_{k'k}$ is the spectral density of the system-bath coupling, v_{nm} denotes the amplitude of the bath-induced modulation of the one-exciton Hamiltonian (i.e., fluctuations of the site energies and intermolecular couplings for $n = m$ and $n \neq m$, respectively), and the brackets indicate averaging over the bath ensemble. We use the simplest possible model of uncorrelated diagonal system-bath interaction with $\langle v_{nm} v_{n'm'} \rangle = v_A \delta_{nm} \delta_{n'm'} \delta_{nn'}$ or $v_B \delta_{nm} \delta_{n'm'} \delta_{nn'}$ if the nth molecule is Chl a or Chl b, respectively. The spectral density was supposed to be the same for Chls a and Chls b, but the corresponding fluctuation amplitudes v_A and v_B were taken to be different. The amplitudes v_A and v_B are dimensionless and take values between 1 and 2, whereas the spectral density is measured in cm^{-1}.

In the Redfield modeling of the intraband relaxation in the B850-LH2[30] and LH1 antenna,[34] the spectral density was taken to have the form $W^2 \exp(-W)$, where $W = \omega_{kk'}/\omega_c$, and ω_c is the characteristic frequency, which was varied around 50 cm^{-1}, and the peak of the spectral density lies at $\omega_{kk'} = 2\omega_c = 100$ cm^{-1}. Besides this low-frequency peak, the real spectral density contains intense resonance peaks at higher frequencies,[35,38,39] but this high-frequency part does not contribute significantly to the intraband relaxation in LH1/LH2. Hence, a spectral density function that consisted of the approximation of the low-frequency part with a simple shape, allowed a quantitative explanation of the wavelength-dependent relaxation dynamics.[34]

For modeling systems with intra- and interband transfers, such as Chl b/Chl a LHCII or the B800–B850 LH2 antenna (both with an interband splitting of about 500–1000 cm^{-1}, depending on the particular pair of levels), more complicated spectral densities are needed. For example, the Chl $b \rightarrow$ Chl a or B800$\rightarrow$B850 transfers may involve coupling to a 750 cm^{-1} vibration as was suggested in earlier hole-burning studies.[40] The simplest form of the spectral density function in such a model must be at least a two-component one, such as the form of eq A11 for example. The positions and relative amplitudes of the low- and high- frequency components (together with the zero frequency amplitude) are given by the parameters V_1, V_2, V_0, ω_{c1}, and ω_{c2} (see eq A11), which are variable in our modeling. In the Discussion section, we compare this definition of spectral density with others.

The static disorder is modeled by repeating the calculation many times (10000 for linear spectra and 500–1000 for nonlinear responses) for a combination of random shifts of the site energies taken from a Gaussian distribution with a fwhm of σ. We take the diagonal disorder to be uncorrelated. To account for a possible difference in the site inhomogeneity value for Chls a and Chls b we introduced amplitude correction factors, with $\sigma_A = s_A \sigma$ and $\sigma_B = s_B \sigma$. The relative amplitudes of the static disorder s_A and s_B are dimensionless factors (near unity), whereas the site inhomogeneity value σ is measured in cm^{-1}.

TABLE 1: Antenna Models (1−4) Allowing to Obtain a Self-Consistent and Quantitative Fit of the Linear Spectra (OD and LD), Superradiance, and Nonlinear Kinetics (TA, TG, and 3PEPS)[a]

1. $A_3 A_6 A_7 B_3 = abab$
   assignment: *aaaaaba abbbb*
   orientations: 0000000 00100
   E (14855 14825 14910 14800 14990 15370 14960 15125 15440 15430 15400 15430) cm^{-1}
   $(s_A\ s_B\ \nu_A\ \nu_B) = (1.0\ 1.0\ 1.2\ 1.85)$
   $(\omega_{c1}\ \omega_{c2}\ V_1\ V_2\ V_0\ \sigma) = (40\ 450\ 9\ 66\ 60\ 170)\ cm^{-1}$

2. $A_3 A_6 A_7 B_3 = baab$
   assignment: *aabaaaa abbbb*
   orientations: 0000000 00100
   E (14875 14875 15450 14830 14925 14920 14925 14875 15430 15450 15430 15440) cm^{-1}
   $(s_A\ s_B\ \nu_A\ \nu_B) = (1.2\ 1.0\ 1.0\ 1.4)$
   $(\omega_{c1}\ \omega_{c2}\ V_1\ V_2\ V_0\ \sigma) = (40\ 550\ 5\ 160\ 60\ 140)\ cm^{-1}$

3. $A_3 A_6 A_7 B_3 = bbaa$
   assignment: *aabaaba ababb*
   orientations: 0010000 00110
   E (14850 14890 15400 14840 14840 15400 14890 14930 15400 15040 15470 15400) cm^{-1}
   $(s_A\ s_B\ \nu_A\ \nu_B) = (1.0\ 1.0\ 1.2\ 1.6)$
   $(\omega_{c1}\ \omega_{c2}\ V_1\ V_2\ V_0\ \sigma) = (40\ 550\ 8\ 135\ 80\ 155)\ cm^{-1}$

4. $A_3 A_6 A_7 B_3 = baba$
   assignment: *aabaaab ababb*
   orientations: 0000000 00100
   E (14865 14865 15410 14820 14960 14920 15430 14920 15430 15010 15410 15440) cm^{-1}
   $(s_A\ s_B\ \nu_A\ \nu_B) = (1.0\ 1.2\ 1.0\ 1.8)$
   $(\omega_{c1}\ \omega_{c2}\ V_1\ V_2\ V_0\ \sigma) = (40\ 550\ 5\ 105\ 50\ 170)\ cm^{-1}$

[a] Assignments (*a* or *b*), orientations (in Gülen's notations), and the site energies E for Chls at sites ($A_1\ A_2\ A_3\ A_4\ A_5\ A_6\ A_7\ B_1\ B_2\ B_3\ B_5\ B_6$) are given for each of these four configurations together with the parameters of the static and dynamic disorder determined from the fit of the experimental data.

Results

The results of our fitting are summarized in Table 1. We found four configurations, nos. 1−4 in the table (*abab*, *baab*, *bbaa*, and *baba*), which can provide a good explanation for the linear spectra (OD and LD), the superradiance, and the nonlinear kinetics (TA, TG, and 3PEPS). The fit results are shown in Figures 1−4 and 7 and 8. For the remaining four configurations we were not able to find any combination of orientations and site energies that gave a good simultaneous fit of linear spectra and nonlinear responses.

Linear Spectra. The simulated 77K OD/LD spectra for the best four configurations are shown in Figures 1−4 together with the experimental spectra (data taken from ref 41). All four configurations gave a good fit of the shape of the linear spectra. In particular, we can reproduce the shoulder of LD at 660−665 nm better than in previous works (e.g., ref 10). We also reproduce the shoulder of OD at 670 nm, and the LD in the Chl b region without any additional rotations of Chls b, in contrast to the model of İşeri and Gülen.[10] The small OD shoulder at 660 nm is a very intriguing feature. Selective excitation at this wavelength results in the slow (2−5 ps) excitation transfer to the 670−680 region, which is usually ascribed to transfer from a monomeric blue-most Chl a.[16,18] Shifting the energy of any Chl a to 660 nm led to serious problems with the fitting of the 660−665 nm region of LD, resulting in a big negative LD peak. The only exception is the *abab* configuration, for which $B_1(a)$ is blue-shifted to $E = 15125$ cm^{-1}. This configuration allowed us to obtain the best OD/LD fit (Figure 1). In the *bbaa* and *baba* models, the blue-most pigment is $B_3(a)$ with $E = 15040$ cm^{-1} and 15010 cm^{-1}
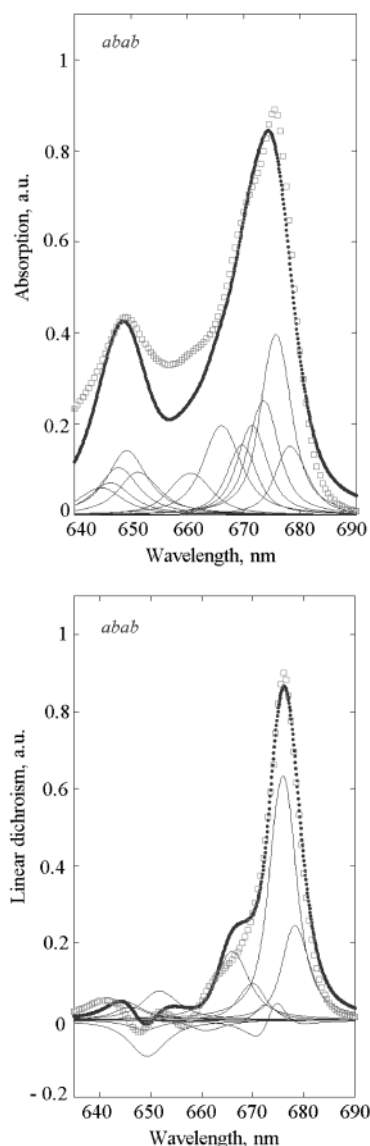
Figure 1. Linear OD and LD spectra for LHCII at 77K. Experimental data (squares) is taken from van Amerongen et al.[41] Calculated data (individual exciton components and the resulting spectra shown by solid lines and points, respectively) was obtained using the exciton model with the static disorder and the homogeneous line widths determined from the Redfield relaxation theory. Parameters are listed in the Table 1, configuration 1 ($A_3A_6A_7B_3 = abab$).

Figure 2. The same as in Figure 1, but for configuration 2 ($A_3A_6A_7B_3 = baab$).

respectively, with a somewhat less good simulated LD spectrum. However, this blue-shifted B_3 does result in a slow ps component of the $a-a$ equilibration, whereas for the $abab$ model we do not find such a slow $a-a$ component (see Figures 9 and 10 and discussion below). The shift of the blue-most Chl a component in the $baab$ model has an excitonic origin, due to significant delocalization between A_1 and B_1 (see Figure 6) and does not give a slow $a-a$ component either (see Figures 9 and 10).

Altogether, according to our experience, the 660−665 nm region is the most critical and most difficult in the OD/LD fitting. This is also the case in the model of İşeri and Gülen.[10] Our four configurations show a reasonable compromise, whereas any other configurations or site energy combinations that do match most other criteria invariably result in a deep negative LD peak in this region. Mixed models with fractional contributions from such configurations will display the same problem.
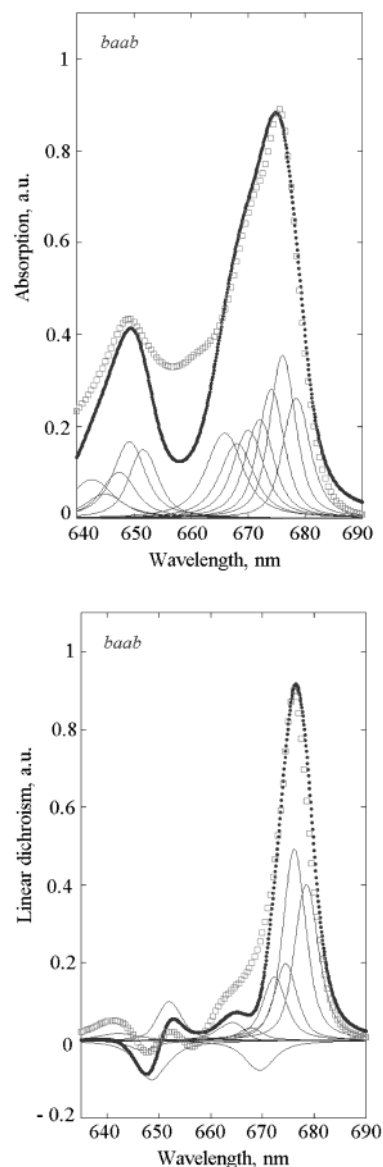
It should be mentioned here that there is a fundamental problem with fitting the LD spectrum of LHCII on the basis of the Kühlbrandt model. We have not calculated an absolute value for the LD in our modeling, but it was found by one of us during previous calculations (van Amerongen, unpublished results) that, for any combination of the orientations given by Kühlbrandt (including the 90° rotated orientations), the calculated LD spectrum is at least twice as small as the experimental LD spectrum. This indicates that the Chl Q_y dipole moments, and possibly the Chl porphyrin planes, should generally lie more parallel to the membrane plane. In view of this uncertainty, it cannot be excluded that a different combination of site energies and Chl identities than the ones we find can provide a good qualitative as well as quantitative fit to the LD spectrum. However, we will assume for the sake of simplicity that the real Chl orientations will be reasonably close to the ones we use except for a rotation toward the membrane plane, and, consequently, that the configurations we find are preferable over ones that give a very bad LD match.

Note that the Redfield theory gives only a homogeneous (Lorentzian) broadening of the spectral lines induced by a weak coupling to the bath. A more realistic line shape theory, taking
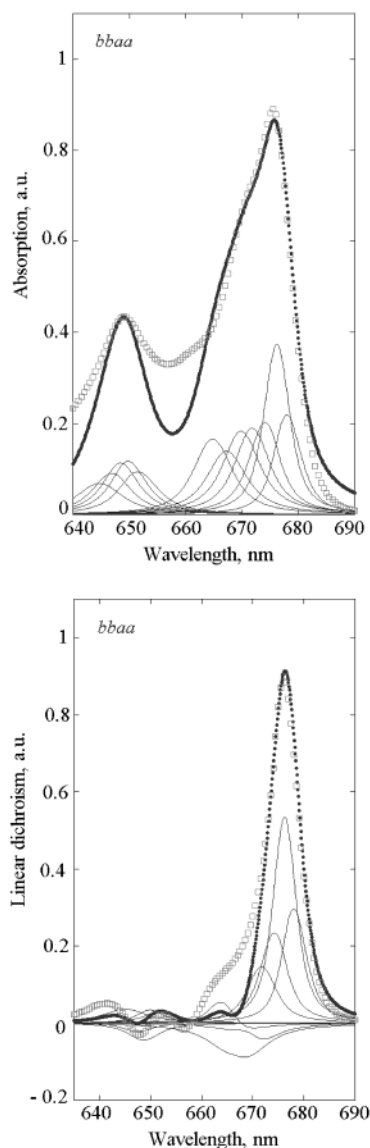
Figure 3. The same as in Figure 1, but for configuration 3 ($A_3A_6A_7B_3$ = *bbaa*).

Figure 4. The same as in Figure 1, but for configuration 4 ($A_3A_6A_7B_3$ = *baba*).

into account the asymmetric phonon and vibrational wing, would yield a better fit of the experimental spectra.

Delocalization of the Exciton Eigenstates and Superradiance. Figures 1−4 show that our four selected configurations all have a very similar exciton structure. The dipole strength is more or less uniformly distributed over 7 exciton states in the Chl *a* region and over 5 states in the Chl *b* region. There are no forbidden states and no highly superradiant states. The most intense transition is the second state in increasing order of energy, which peaks at 675−677 nm, and its dipole strength is no more than 1.5−2 times the monomeric dipole strength. We remind that the existence of a state with a dipole strength of 2.3 ± 0.8 was suggested by nonlinear absorption/nonlinear polarization studies in the 670−690 nm region.[13]

Due to the nonparallel orientation of the monomeric dipoles, the dipole strength enhancement of an individual exciton state is generally smaller than the delocalization length. Therefore, we provide a direct estimate of the degree of delocalization of the exciton eigenstates in Figure 5, plotting the participation ratio of the wave functions $\sum_n (c_n^k)^4$ versus wavelength of the *k*th state after averaging over the disorder. For all four configurations, the participation ratio is between 0.4 and 0.6 in the Chl *a* region and 0.6−0.8 in the Chl *b* region. The
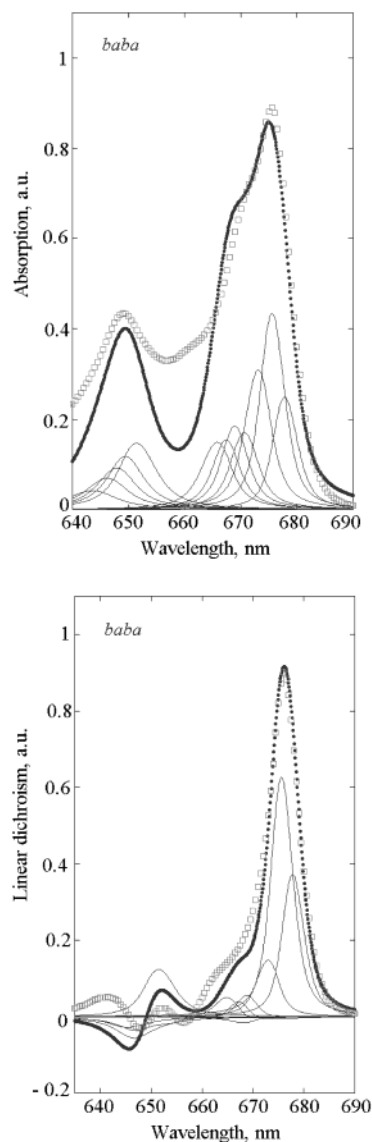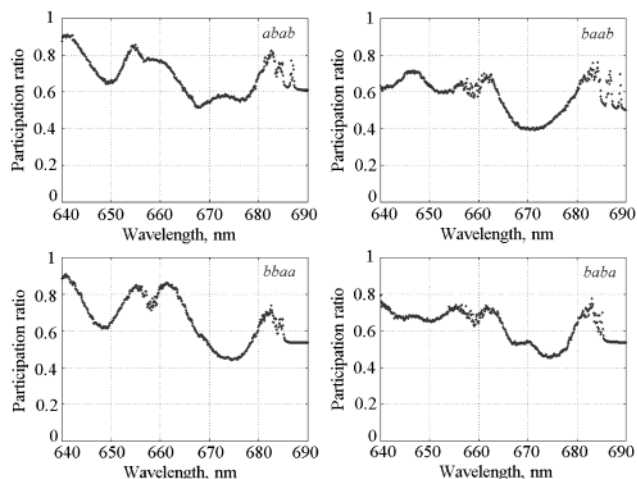

Figure 5. The participation ratio of the exciton wave functions at 77K as a function of the wavelength calculated for the $A_3A_6A_7B_3$ = *abab*, *baab*, *bbaa*, and *baba* configurations. Parameters are the same as those in Figures 1−4 (see also Table 1).

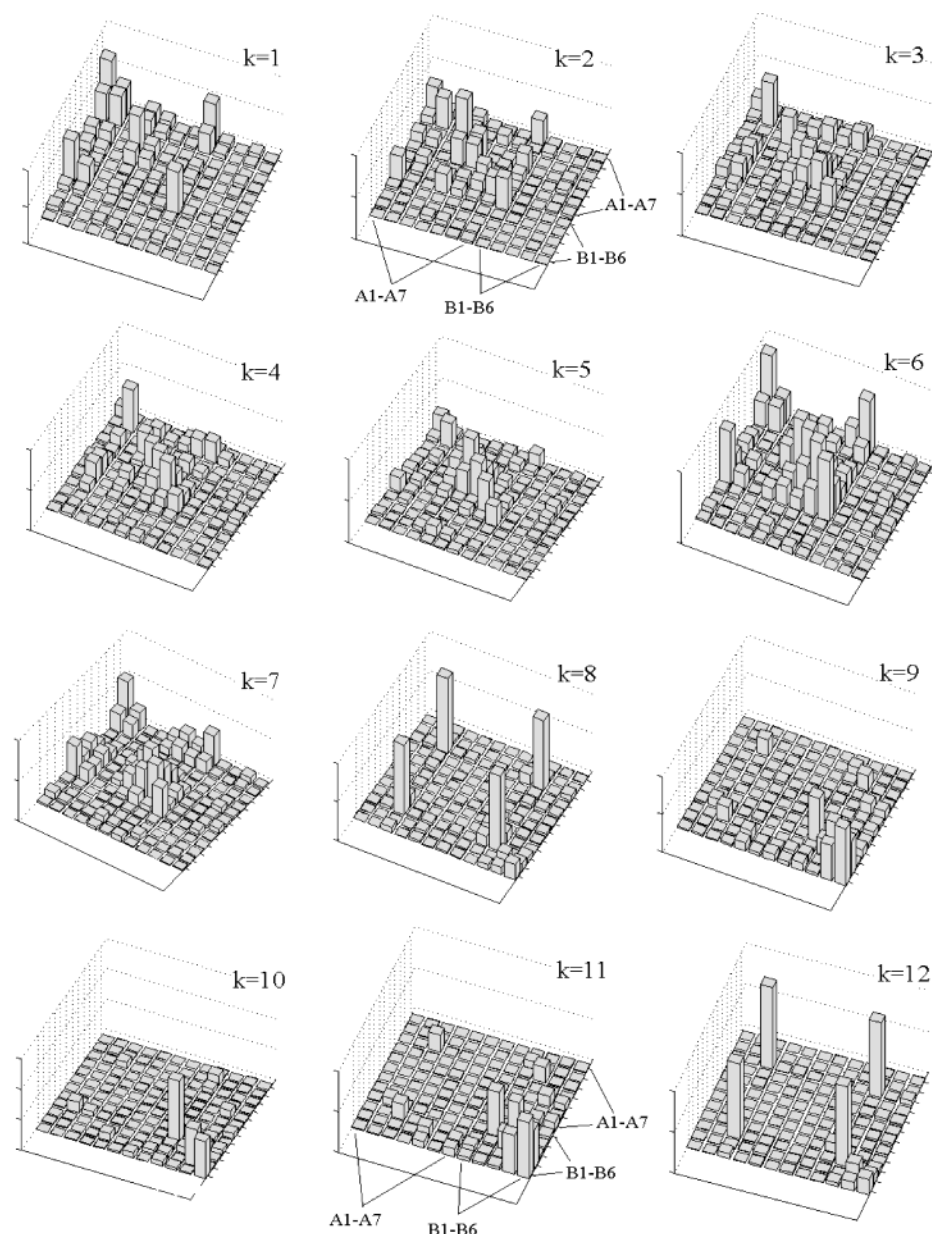corresponding degree of delocalization is 2 ± 0.5 and 1.4 ± 0.3, respectively.

Figure 6. The absolute values of the density matrix for the pure exciton states ($k = 1$ to $k = 12$, configuration 2, $A_3A_6A_7B_3 = baab$) averaged over disorder. The diagonal elements $\rho(n,n)$ for any fixed k give the population of the nth site in the kth exciton state, the off-diagonal elements $\rho(n,m)$ correspond to a coherence between nth and mth sites in the kth exciton state. The sites are numbered in the following order: A_1, A_2, A_3, A_4, A_5, A_6, A_7, B_1, B_2, B_3, B_5, B_6. The exciton states are numbered in the increasing order of energy, i.e., the $k = 1$ panel gives the density matrix of the lowest state averaged over realizations of the static disorder, etc.

At 77K the intense second state is thermally mixed with the weaker lowest state and we calculate the superradiance to be 1.09 for configuration *abab*, 1.16 for *baab*, 1.13 for *bbaa*, and 1.22 for *baba*. These values are in good agreement with the experimental value of 1.16 ± 0.07 obtained for LHCII at 77K.[14]

More detailed information about the exciton states can be obtained from the density matrix picture. Figure 6 shows the 12 density matrixes for the pure exciton states (from $k = 1$ to $k = 12$), averaged over disorder, for the *baab* configuration. For any fixed k, the diagonal elements $\rho(n,n)$ of the matrix give the population of the nth site in the kth exciton state, and the off-diagonal elements $\rho(n,m)$ correspond to the coherence between the nth and mth sites in the kth exciton state. For example, the lowest exciton state, $k = 1$ (top left), is characterized by a strong coherence between sites A_1, A_2, and B_1, as can be seen from the off-diagonal elements connecting the first, second, and eighth sites. Some coherence is also present between

sites A_4 and A_5, but there is almost no coherence between this cluster and the $A_1-A_2-B_1$ cluster. This means that the $k = 1$ state is a noncoherent mixture of two delocalized excitons, i.e., depending on the realization of the disorder in a particular complex, the lowest state is either the $A_1-A_2-B_1$ or the A_4-A_5 exciton. A similar situation is observed for the $k = 2$ state, but with less coherence between A_1 and A_2 and some additional coherence between A_4 and B_1. For the $k = 3$ state, the delocalized $A_6(a)-A_7(a)$ exciton is noncoherently mixed in. The higher Chl a states are an increasingly incoherent mixture of all Chl a sites, except for $k = 6$ which is strongly dominated by an A_1-B_1 coherence, the upper exciton counterpart of $k = 1$.

The states from $k = 8$ to $k = 12$ correspond to excitation of the Chl b region. Here, delocalization occurs within the B_3-$(b)-A_3(b)$ and B_5-B_6 dimers, and we have a localized B_2 state. Within each Chl b exciton state, we observe noncoherent

LHCII Complex of Higher Plants

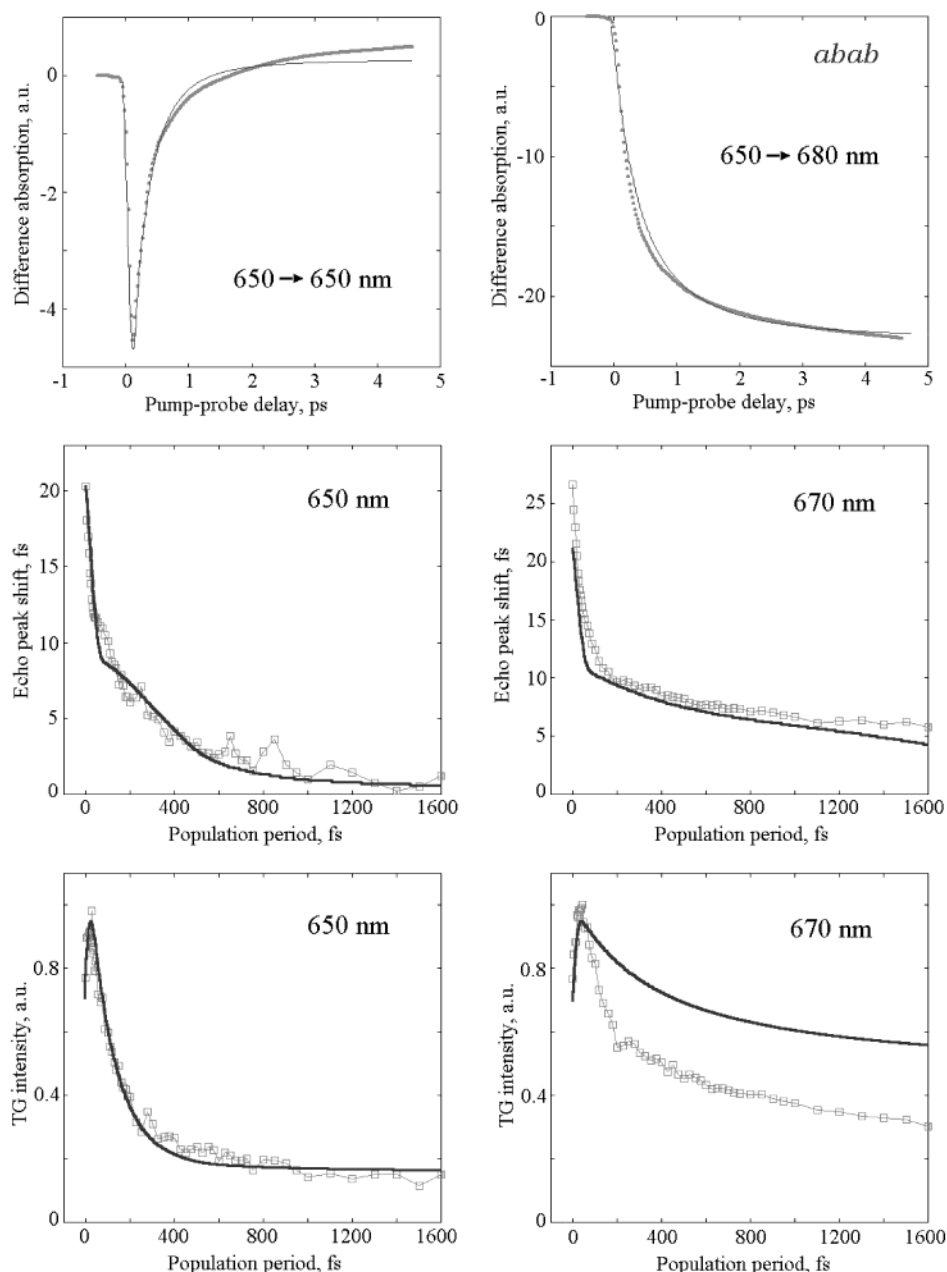*J. Phys. Chem. B, Vol. 107, No. 8, 2003* **1899**

Figure 7. Transient absorption (TA), three-pulse photon echo peak shift (3PEPS) and transient grating (TG) kinetics for LHCII at room temperature. Experimental TA kinetics at 650 and 680 nm upon 650 nm excitation shown in the top frames (points) are reproduced from Connelly et al.[22] Experimental 3PEPS and TG kinetics measured at 650 and 670 nm shown in middle and bottom frames (squares connected by thin solid line) are taken from Salverda et al.[24] Calculated data (solid lines) is obtained for $A_3A_6A_7B_3 = abab$ configuration using the Redfield theory with the parameters listed in Table 1. In the TA fitting the pump and probe pulse duration is 65 and 80 fs, respectively, to reproduce the experimental conditions. In the 3PEPS/TG fitting the pulse duration is 35 fs.

superposition of all these clusters. Some coherence between Chls a and Chls b can also be discerned in the Chl b state matrixes, especially for states $k = 9-11$ where an off-diagonal A_2-B_2 element is clearly present. The Chl a−Chl b coherence is also quite pronounced in the upper Chl a state $k = 7$, with off-diagonal elements connecting almost all Chl a sites with B_5. In other Chl a states there is some coherence between the Chl a sites A_5, A_7 and the Chl b sites B_5, B_6. Note that the *baab* configuration is the most delocalized one of the four we have found. In other configurations (data not shown), the B_3-A_3 and A_6-A_7 coherences are broken, with A_3 or B_3 turned into a Chl a, and with A_6 or A_7 turned into a Chl b.

Kinetics of the Nonlinear Response. In Figures 7 and 8, simultaneous fits of the room-temperature TA, 3PEPS, and TG kinetics are shown. The transient absorption is probed in the

middle of the Chl b and Chl a bands at 650 and 680 nm, respectively, after 650 nm excitation (data reproduced from ref 22). In the three-pulse photon echo experiment (data reproduced from ref 24), the TG and 3PEPS signals are obtained with 18 nm fwhm pulses centered at 650 or 670 nm. The fit is shown for the *abab* and *bbaa* configurations, which gave the best quantitative agreement.

The interpretation of the TA kinetics is straightforward. Impulsive excitation at 650 nm creates population on the Chl b sites, which subsequently is transferred to the Chl a sites with one picosecond and several sub-picosecond time constants. This transfer is displayed as the decay of the TA signal at 650 nm, mirrored by the increase of the 680 nm signal. The situation is slightly more complicated due to the appearance of excited-
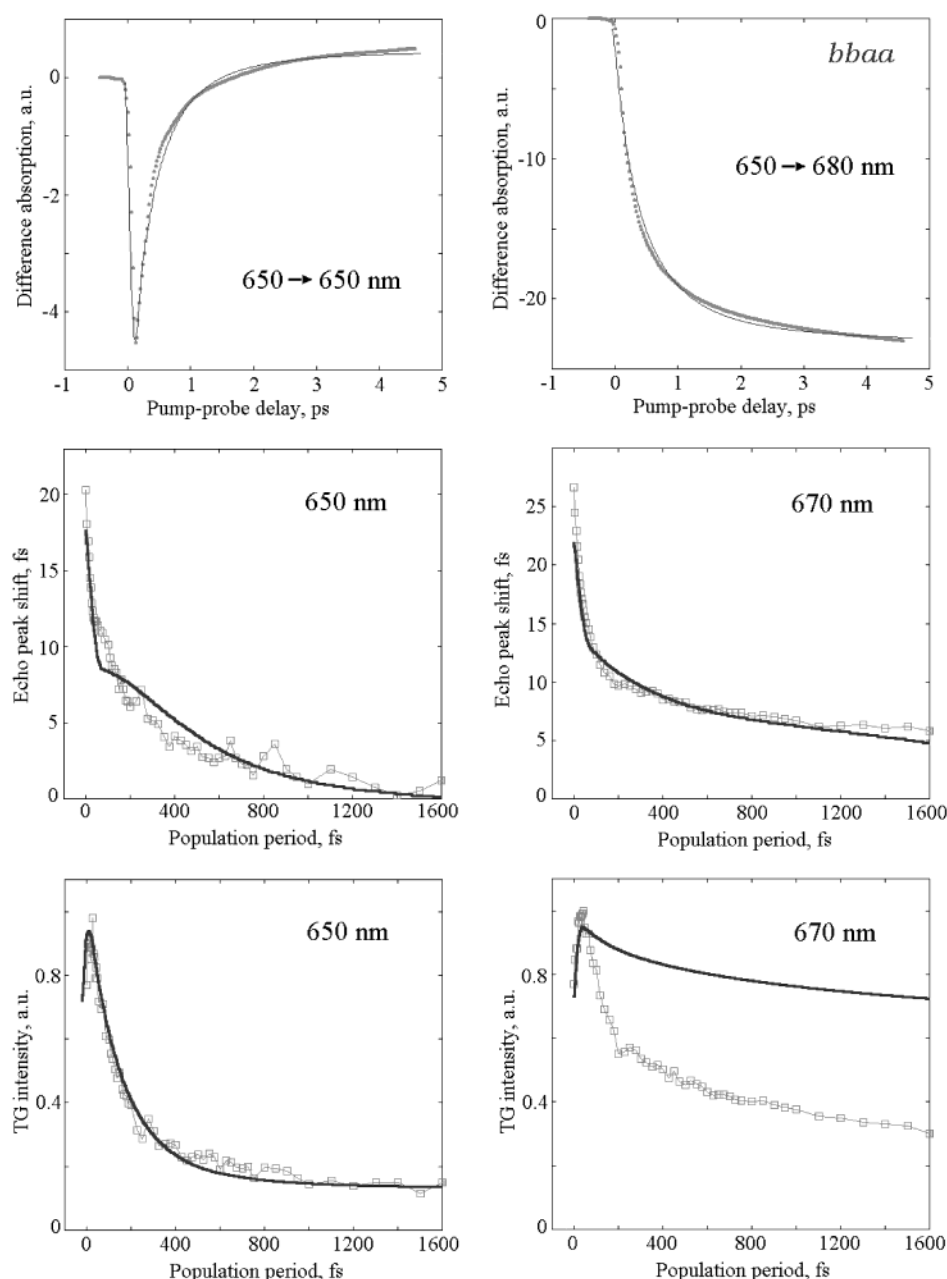
Figure 8. The same as in Figure 7, but for $A_3A_6A_7B_3 = bbaa$ configuration.

state absorption from the Chls *a* at 650 nm, but this is a minor effect.

The TG decay at 650 nm looks very similar to the TA decay at the same wavelength, which suggests that it is mainly determined by Chl *b*→Chl *a* transfer. Indeed, the TG signal is known to be sensitive to transfer out of the laser spectral window ("interband"), and not to transfer within laser window ("intraband"), in contrast to 3PEPS which is used to probe the latter type of transfer. However, this insensitivity of TG to intraband transfer only holds for transfer between identical molecules with parallel transition dipoles, or for transfer between delocalized states which have the same energies and dipole orientations. In the case of intraband transfer between states with different dipole orientations, the TG intensity will decrease due to depolarization. On the other hand, irreversible migration to a low-lying state (within the laser window) with the same polarization leads to an increase of TG intensity, because the $|P|^2$ factor (see eq A3 in the appendix) for a single state is bigger than the sum of such factors for a noncoherent superposition of several states.

As a result intraband transfer may give rise to a complicated TG signal as a function of the population period T. Typically, the TG intensity decreases for a disordered system like LHCII, but the amplitude of this decrease is relatively small. In contrast, transfer out of the laser window has a dramatic effect. For example, the interband migration of localized excitations reduces the TG intensity to zero, with $S_{TG}(T) = S_{TG}(0)\exp(-2\gamma T)$, where γ is the rate constant corresponding to the transfer. In the delocalized case, the TG intensity often does not decay to zero, due to a bleaching contribution from the ground state of a site which contributes to both the in-band and out-of band states. For a dimer, the interband relaxation, or relaxation to a dark exciton state, of a delocalized excitation yields $S_{TG}(T) = S_{TG}(0)[1 + 2\exp(-\gamma T) + 2\exp(-2\gamma T)]$. For LHCII, it can be shown that in the absence of interband Chl *b*→Chl *a* transfer, the TG at 650 nm shows only a relatively small slow component, reflecting the intraband Chl *b*→Chl *b* transfer. Switching on the Chl *b*→Chl *a* transfer results in a fast component with large amplitude in agreement with the measured data. Both measured

LHCII Complex of Higher Plants

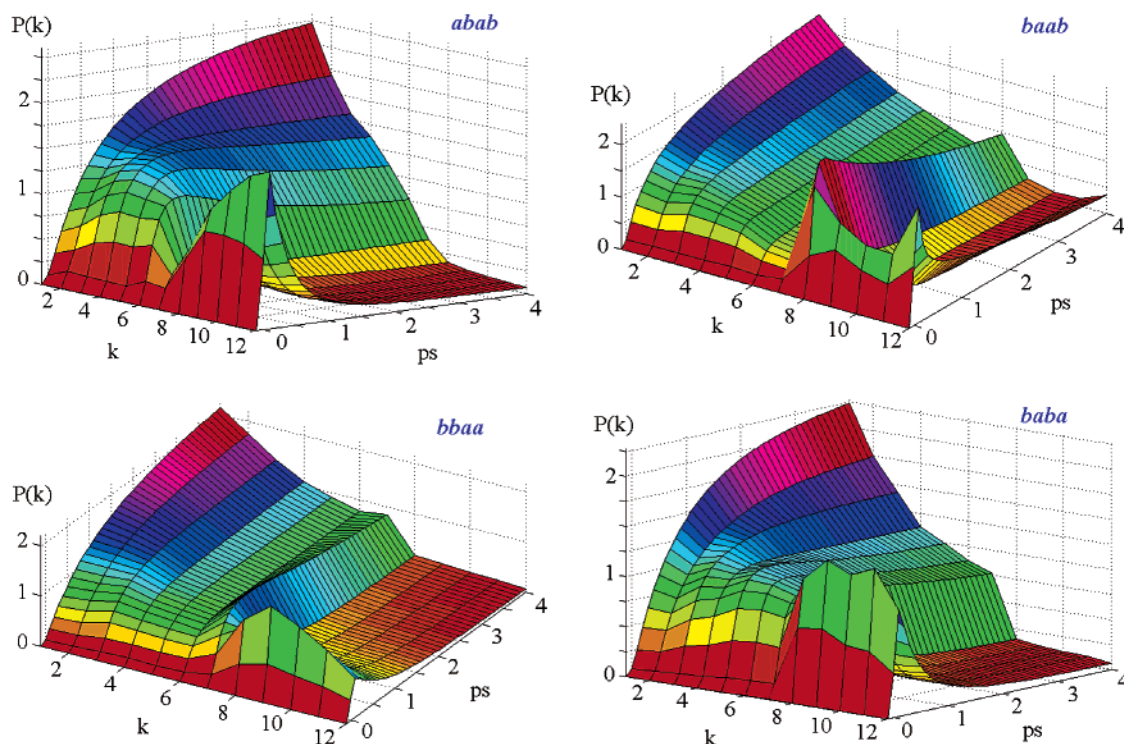*J. Phys. Chem. B, Vol. 107, No. 8, 2003* **1901**

Figure 9. Kinetics of the exciton state populations $P(k)$ for the *abab*, *baab*, *bbaa*, and *baba* models upon excitation of the Chl *b* band. Populations are given in arbitrary units, k denote the number of exciton states from 1 to 12 in increasing order of energy, time delays from −100 fs to 4 ps are shown with the 100 fs step. Excitation wavelengths and pulse durations are 640 nm and 60 fs (*abab* and *baab*), 650 nm and 120 fs (*bbaa*), and 645 nm and 120 fs (*baba*). Parameters are listed in Table 1 (room temperature).
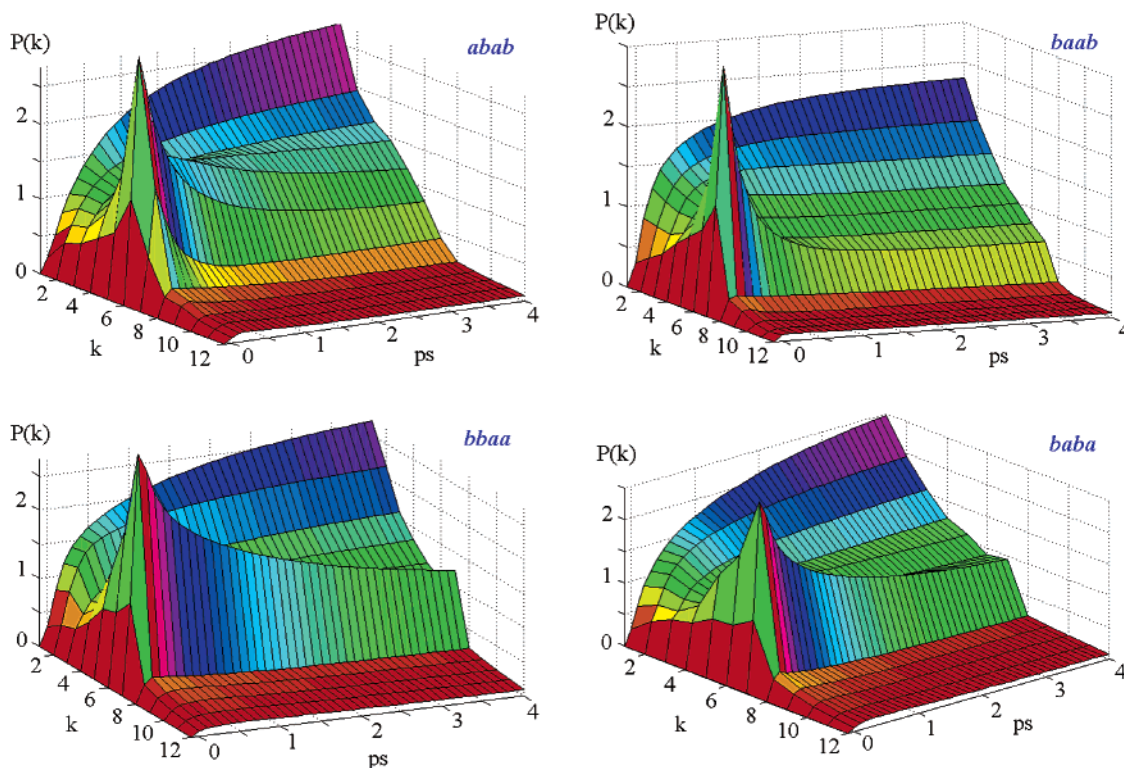
Figure 10. The same as in Figure 9, but upon selective excitation of the upper exciton state ($k = 7$) of the Chl *a* band. Excitation wavelength is 663 nm, pulse duration is 120 fs.

and calculated TG curves show a nonzero final level which is reached after the energy transfer is complete. This residual TG value may originate from the bleaching of a common ground state, due to coherence between the Chl *a* and Chl *b* sites, or from one-exciton resonances of the Chl *a* states which overlap

with the broad 650 nm laser pulse, or from blue-shifted one-to-two-exciton resonances of the Chl *a* states (excited-state absorption).

The 3PEPS kinetics at 650 nm looks rather different from the TG decay, which suggests that it indeed reflects the intraband

1902 *J. Phys. Chem. B, Vol. 107, No. 8, 2003*

Novoderezhkin et al.

Chl b→Chl b dynamics. However, the intraband Chl b→Chl b dynamics is strongly influenced by Chl b→Chl a transfer, because the distribution of population among the Chl b states is controlled not only by slow b→b transfer but also by strong, essentially nonuniform, connections of these states to Chl a states. A a consequence, the 3PEPS dynamics at 650 nm is significantly influenced by Chl b→Chl a transfer. This nondirect effect of interband transfer on the 3PEPS dynamics was originally pointed out by Agarwal et al.[23] A 650 nm 3PEPS curve, which we have calculated with the Chl b→Chl a transfer artificially switched off (not shown) looks very similar to the 3PEPS at 670 nm, with larger peak shift values, and only the fast coherent artifact followed by slow dynamics. In the absence of any transfer, both calculated 650 and 670 nm 3PEPS curves still show the sharp peak within 60−80 fs delays determined by the coherent artifact, but this is followed only by a constant peak shift value of about 9−12 fs (depending on parameters).

The TG kinetics at 670 nm is difficult to explain quantitatively by our model. In contrast to the 650 nm case, we find no interband transfer out of the laser window, as even the lowest state is within reach of our pulse. Hence, we cannot explain the large decrease in the TG amplitude which was observed both by Salverda et al.[24] and by Agarwal et al.[23] The maximal decrease of the TG amplitude due to depolarization induced by transfer between chromophores within the laser window is $S_{TG}(\infty)/S_{TG}(0) = {}^4/_9$ for relaxation between perpendicularly polarized transitions with close frequencies and ${}^8/_9$ in the case of well separated frequencies. For parallel transition dipoles $S_{TG}(\infty)/S_{TG}(0) = 1$, or even more than unity if the transition energies are different. In the Chl a band, the transitions have different orientations and both overlapping and separated absorption bands, and we calculate an average value of $S_{TG}(\infty)/S_{TG}(0)$ of about 0.5−0.7. However, the experimental value is significantly less, suggesting that the TG decay at 670 nm has to be due to flow of some emitting strength out of the laser window. This could be because of some slow nuclear relaxation, giving rise to a dynamic Stokes shift of the lowest exciton states. More likely, the lowest 1 or 2 states are not within reach of the laser pulse to begin with. Accounting for this by narrowing the pulse in our calculations led only to a less good match for 3PEPS without better agreement for the transient grating. The lowest states probably have to be actually red-shifted. This is also suggested by the difference between the 77 K and the room-temperature absorption spectrum, with the latter having a much larger red shoulder (see ref 42 for a detailed comparison). A preliminary calculation for which we shifted the site energies of the reddest Chls a to 680 nm or below (not shown) indicates that the TG decay amplitude can be significantly increased in that way without affecting the peak shift decay.

The 670 nm peak shift decay is reproduced very well in our simulations. Both slow and fast transfer processes between all or nearly all the Chl a exciton states will be contributing to this decay. Even if the reddest states do not overlap as well with the laser pulse, they will still have an effect on the distribution of population among the higher Chl a states, thus indirectly affecting the peak shift, analogous to the 650 nm case.

Energy Transfer Rates. The fitting of the nonlinear responses with the Redfield theory approach provides us with information about the time scales and pathways of excitation energy transfer in the LHCII antenna. The Redfield relaxation tensor consists of the rates of relaxation/energy transfer between every pair of exciton eigenstates. The density matrix unravels the structure of these eigenstates, which can be localized at a particular site, or delocalized over a few sites. By carefully studying the relaxation tensor and the density matrixes together, we can distinguish between exciton relaxation and site-to-site migration of excitation, and estimate the corresponding rate constants. Unfortunately, the picture is complicated by the noncoherent mixing of eigenstates due to disorder. Therefore, we will start by analyzing the case of one particular realization of the site energies. The example in Table 2 shows the rates of population transfer $R_{k'k'kk}$ and the squared wave function amplitudes c_{nk}^2 for such a realization of the static disorder for the *bbaa* configuration. The transfer rate $R_{k'k'kk}$ is proportional to the wave function overlap, i.e., $\sum_n c_{nk}^2 c_{nk'}^2$. This means that, for efficient transfer from state k, mainly localized on site m, to state k', mainly localized on site n, the wave function of state k, with an amplitude maximum c_{mk}^2, must exhibit at least a sizable wing at the nth site given by c_{nk}^2. Such a wing will be present as a consequence of interaction between the nth and mth sites. In the limit of very weak coupling (the Förster limit), the c_{nk}^2 value can be calculated perturbatively and is proportional to the square of the dipole−dipole interaction energy M_{nm}. The Redfield theory is valid for arbitrary strong intermolecular couplings. Stronger interaction induces more delocalization with more overlap between the wave functions, thus increasing the transfer rate.

Note that in the presence of off-diagonal disorder (modulation of the M_{nm} elements), which we did not consider, additional contributions will be present such as $\sum_{nm} c_{nk}^2 c_{mk}^2$, with a large c_{mk} amplitude instead of a small c_{nk} value only. This can significantly increase the rate of k→k' transfer at fixed $J_{k'k}$. Similarly, a correlation between the fluctuations at the nth and mth sites will give rise to additional terms, such as $\sum_{nm} c_{nk} c_{mk} c_{nk'} c_{mk'}$, which can affect the transfer rate.

From the distribution of the wave function amplitudes shown in Table 2 (bottom), we can determine the interacting sites which are responsible for relaxation/migration between a particular pair of exciton states. In the Chl b band, for this particular realization significant delocalization occurs between $A_6(b)$ and B_6, resulting in an upper and lower dimeric state ($k = 11$ and 12). Next to these, we calculate that three nearly localized states are formed on sites $A_3(b)$, B_2, and B_5. Note that for other realizations of the disorder, the delocalized states can reside on B_5 and B_6, together with a localized state on A_6. In both cases, the intradimer relaxation rate is 2−3 ps^{-1} (transfer time 300−500 fs), whereas transfer from the A_6−B_6 or B_5−B_6 dimer to the Chl a states occurs with a time constant of 500−800 fs, as can be seen in the middle of columns $k = 11$ and 12 in Table 2. Migration between the localized Chl b states occurs on a picosecond time scale, but the transfer from these localized Chl b states to the Chl a states is very fast, so effectively they are almost disconnected from each other. Specifically, the $B_2(b)$−$A_2(a)$ interaction (see column $k = 10$ in Table 2) results in fast transfer with a 120−190 fs time constant, the $A_3(b)$−$B_3(a)$ interaction (column $k = 9$) induces Chl b population decay with a time constant of about 200−300 fs, and $B_5(b)$−$A_5(a)$ coupling (column $k = 8$) results in 1.2−1.8 ps b→a transfer. For realizations with a localized A_6 state, the $A_6(b)$−$A_7(a)$ interaction leads to a 500−600 fs component. For almost all realizations, the exciton states are similar in nature, except for the energy ordering, and also the relaxation time scales lie approximately within the ranges given above. In a few cases, complicated B_5−B_6−A_6 coherent mixing results in three delocalized states with sub-picosecond relaxation.

In the Chl a region, either the highest state, $k = 7$, or the state $k = 6$ is always almost completely localized on the most blue-shifted pigment $B_3(a)$. The $B_3(a)$ state is only weakly

LHCII Complex of Higher Plants

J. Phys. Chem. B, Vol. 107, No. 8, 2003 **1903**

TABLE 2: The Population Relaxation Rates, $R_{k'k'kk}$ (ps^{-1}), and the Wavefunction Amplitudes, c_{nk}^2, for One Particular Realization of the Static Disorder for the *bbaa* Configuration (at Room Temperature)^a

						k						
k'	1	2	3	4	5	6	7	8	9	10	11	12
1	**2.419**	−0.096	−0.386	**−2.011**	−0.477	*−1.754*	−0.019	−0.315	−0.010	−0.124	−0.076	−0.043
2	−0.091	**2.743**	−0.454	−0.595	*−1.213*	**−4.050**	−0.027	−0.053	−0.040	−0.326	−0.185	−0.128
3	−0.294	−0.364	1.497	−0.550	−0.084	−0.166	−0.010	−0.080	−0.023	−0.029	−1.280	−1.026
4	**−1.256**	−0.392	−0.451	**3.340**	−0.189	−0.077	−0.013	−0.071	−0.020	−0.099	−0.101	−0.074
5	−0.184	−0.493	−0.042	−0.117	3.274	*−1.081*	−0.044	−0.091	−0.253	−3.847	−0.069	−0.054
6	−0.560	**−1.364**	−0.069	−0.039	−0.897	**7.362**	−0.039	−0.021	−0.120	−1.680	−0.050	−0.036
7	−0.004	−0.006	−0.003	−0.005	−0.028	−0.030	0.799	−0.003	−3.518	−0.309	−0.025	−0.022
8	−0.019	−0.003	−0.006	−0.007	−0.015	−0.004	−0.000	1.017	−0.009	−0.003	−0.295	−0.640
9	−0.000	−0.001	−0.001	−0.001	−0.027	−0.015	−0.596	−0.006	4.450	−0.475	−0.056	−0.051
10	−0.004	−0.011	−0.001	−0.005	−0.333	−0.175	−0.042	−0.002	−0.385	6.906	−0.002	−0.012
11	−0.002	−0.005	−0.048	−0.004	−0.005	−0.004	−0.003	−0.134	−0.038	−0.002	**3.815**	**−2.041**
12	−0.001	−0.003	−0.031	−0.002	−0.003	−0.002	−0.002	−0.237	−0.029	−0.008	**−1.671**	**4.132**
$b{\rightarrow}b$								−0.379	−0.463	−0.490	**−2.026**	**−2.746**
$b{\rightarrow}a$								−0.637	*−3.987*	*−6.416*	−1.789	−1.386
A_1	0.246	**0.491**	0.027	0.000	0.015	**0.217**	0.001	0.000	0.000	0.000	0.000	0.000
A_2	0.014	0.019	0.000	0.017	*0.593*	*0.304*	0.005	0.000	0.003	*0.035*	0.000	0.000
A_3	0.000	0.000	0.000	0.000	0.000	0.000	0.035	0.001	0.904	0.053	0.003	0.002
A_4	**0.154**	0.036	0.164	**0.623**	0.019	0.000	0.000	0.001	0.000	0.000	0.000	0.000
A_5	**0.507**	0.169	0.027	**0.290**	0.000	0.003	0.000	0.002	0.000	0.000	0.000	0.000
A_6	0.000	0.000	0.002	0.000	0.001	0.000	0.000	0.000	0.005	0.000	**0.630**	**0.360**
A_7	0.041	0.118	0.759	0.067	0.001	0.000	0.000	0.000	0.000	0.000	0.009	0.002
B_1	0.033	**0.161**	0.009	0.001	*0.337*	**0.456**	0.001	0.000	0.000	0.000	0.000	0.000
B_2	0.000	0.001	0.000	0.000	0.024	0.011	0.000	0.000	0.054	0.906	0.000	0.001
B_3	0.000	0.000	0.000	0.000	0.002	0.006	0.956	0.000	*0.032*	0.003	0.000	0.000
B_5	0.001	0.000	0.000	0.000	0.001	0.000	0.000	0.974	0.000	0.000	0.009	0.012
B_6	0.000	0.000	0.007	0.001	0.000	0.000	0.000	0.021	0.000	0.001	**0.347**	**0.621**

^{a} The kth column shows the $k{\rightarrow}k'$ relaxation rates. The diagonal elements $R_{kkkk} = -\sum_{k'} R_{k'k'kk}$ correspond to the inverse lifetime of the kth level. For the b states ($k = 8-12$) the sums of the $b{\rightarrow}b$ and $b{\rightarrow}a$ transfer rates are shown in a two separate rows. The total rate of the b states decay (diagonal elements of the b block) equals to the sum of these two rows. The square of the wave function amplitudes shows a participation ratio of the nth site (from A_1 to B_6) in the kth exciton state. The wave function amplitudes and relaxation rates are shown by bold in the case of strong exciton coupling and are underlined for localized states. The italicized values are the transfer rates corresponding to the hopping between delocalized clusters with one common site. The italic bold values correspond to special cases when relatively small wave function overlap is combined with strong system-bath coupling (very fast $b{\rightarrow}a$ transfer with the difference of energies corresponding to the maximum of spectral density) or when large overlap occurs between close states (resulting in a relatively slow transfer in the a region).

coupled to the other Chl a states, and strongly coupled to the Chl b state which involves the $A_3(b)$ site ($k = 9$ in our example). $B_3(a)$ has a ps lifetime, with the main relaxation path corresponding to uphill transfer to the A_3 state, and is expected to be a bottleneck in the Chl $b{\rightarrow}$Chl a transfer upon 650 nm excitation. Its long lifetime could well be the origin of the slow ps kinetics observed upon narrow-band excitation near 663 nm.[16,18] Another state is localized on $A_7(a)$ and also gives rise to a relatively long-lived state. In our example, this is $k = 3$ with a 700 fs lifetime, still rather shorter than the observed time constants of several ps for blue-side Chl a excitation which are observed. Significant delocalization between B_1 and A_1 (dimeric states $k = 2$ and 6), and that between A_4 and A_5 (dimeric states $k = 1$ and 4), results in fast relaxation of the upper exciton states $k = 4$ and 6, with inverse relaxation rates of 500 and 250 fs, respectively. We also observe strong B_1–A_2 coupling, resulting in the delocalized $k = 5$ and 6 states, but the corresponding relaxation rate is not very high, which is due to the small splitting between these levels in this particular realization. The spectral density we have chosen for our model increases with frequency from zero value and reaches a maximum at high frequencies corresponding to the Chl b–Chl a energy gap. This spectral density function allows us to explain the large rates of Chl $b{\rightarrow}$Chl a transfer even though the overlap of the exciton wave functions is rather small, amounting to 0.03−0.04 for the strongest interactions, in the $B_2(b)$–$A_2(a)$ and $A_3(b)$–$B_3(a)$ pairs (see column $k = 9$ and 10 in Table 2). Note again that, in the case of off-diagonal dynamic disorder

(i.e., modulation of the B_2–A_2 and A_3–B_3 couplings) or of correlated diagonal disorder (correlated fluctuations of the site energies for the B_2–A_2 and A_3–B_3 pairs), we would need a different spectral density amplitude at high frequencies than the one we used, to obtain equally fast interband transfer.

On the other hand, the Chl $a{\rightarrow}$Chl a transfer is characterized by low spectral density values combined with large wave function overlap. Together, these result in the above-described sub-picosecond exciton relaxation within the B_1–A_1, B_1–A_2, and A_4–A_5 dimers, and the fast hopping between these spatially separated dimers, or more complicated clusters. Consequently, the $k = 5$ to $k = 2$ transfer in our example corresponds to hopping between the B_1–A_2 and B_1–A_1 dimers with an 1.2 ps^{-1} rate (800 fs time constant). Similarly, the $k = 6$ to $k = 1$ transfer consists of hopping between the B_1–A_2–A_1 and A_4–A_5–A_1 clusters with a 600 fs time constant (1.8 ps^{-1} rate). Altogether, the combined action of intracluster relaxation and intercluster hopping results in lifetimes of the higher Chl a states of the clusters ($k = 4-6$) of 150−300 fs. It should be noted that the numbers displayed in Table 2 are mainly suited for an identification of the main relaxation/migration pathways corresponding to the most strongly coupled pairs of pigments (or clusters). The true population kinetics, with 12 components for each state, both slow and fast, is difficult to imagine without a direct simulation. We will come back to this in the next subsection.

For the other configurations, the Redfield tensor generally looks similar to the *bbaa* case, except for a few specific

differences which we will highlight here. For the *abab* configuration, we obtain a Chl *b* dimer, which can be B_5–B_6, B_5–A_6, or B_6–A_6, just like that in *bbaa*, with 300–600 fs intradimer relaxation superimposed on the 400–800 fs transfer to the Chl *a* states. In comparison to *bbaa*, the orientation for the B_5 dipole moment is different for this configuration (see Table 1). As a result, the B_5–A_5 coupling is much stronger in *abab*, and the corresponding transfer rates increase accordingly. Thus, transfer to the Chl *a* band takes only 120–250 fs from the dimeric states with a predominant B_5 contribution, which are found in realizations of the disorder with B_5–B_6 or B_5–A_6 dimers. In the other realizations, transfer from the localized B_5 state is also fast, taking about 400 fs, rather than 1.2–1.8 ps as found for the *bbaa* configuration. For realizations of the disorder with localized B_6 or A_6 states, the transfer from there to Chl *a* states occurs with a 400–600 fs time constant, just like in the *bbaa* case. From the localized states on B_3 and B_2, transfer to the other Chl *b* states is even more slow than in the *bbaa* case, taking 3–5 ps or even longer. The excitation is thus transferred rapidly to Chl *a* states, within 250–500 fs from the A_2 state due to coupling to B_2, and within 150–250 fs from B_3 to A_3. In the Chl *a* region, the upper state, $k = 7$, is localized on the most blue-shifted site, B_1 for this configuration. We note that in this configuration the B_1 state does not provide a slow Chl *a* equilibration component, as its lifetime is limited by rapid (~400 fs) relaxation due to B_1–A_1 coupling. This relaxation is followed by a 400–500 fs relaxation within the A_1–A_2 dimer. The A_4–A_5 dimer is characterized by a low degree of delocalization and correspondingly slow intradimer dynamics, with a time scale of 1.2–1.4 ps. The overall lifetimes of the upper Chl *a* states ($k = 3$–7) will be 200–300 fs for the ones which are delocalized over a cluster, and much longer, about 0.6–1.4 ps, for the states which are nearly localized on A_3 or A_7.

The *baab* configuration is characterized by an additional dimer in the *b*-region, on the sites $A_3(b)$ and $B_3(b)$. This dimer is weakly connected with the other Chl *b* states and also with the Chl *a* states, which gives rise to an additional and intense picosecond component in the Chl *b*→Chl *a* transfer. In contrast, the Chl *a*→Chl *a* transfer is very fast, as all Chls *a* are found in strongly coupled clusters, namely, in the A_1–A_2–B_1 cluster, the A_4–A_5 dimer, and the A_6–A_7 dimer (see Figure 6).

For the *baba* configuration, the most important feature is the slow decay of the highest Chl *a* level, the $k = 7$ state which is determined by the blue-shifted $B_3(a)$ site. Altogether, the dynamics in this configuration strongly resemble those found for *bbaa*.

Excitation Dynamics in the Eigenstate Representation. In Figures 9 and 10, we plot the overall dynamics of the exciton state populations, averaged over disorder, for all four configurations. The dynamics upon 650 nm excitation are shown in Figure 9, upon 663 nm excitation in Figure 10.

Excitation of the Chl *b* band by a short 650 nm pulse results in the almost uniform population of the Chl *b* states at zero delay. For the three configurations *abab* (top left), *bbaa* (bottom left), and *baba* (bottom right) the subsequent overall dynamics are very similar. Sub-picosecond population decay of all five Chl *b* states ($k = 8$–12) takes place, mirrored by fast population of the Chl *a* states ($k = 1$–7), and followed by a slower picosecond equilibration in the Chl *a* region (see also the previous subsection).

For the *baab* configuration (top right), the dynamics are clearly different. After 100 fs, the population of states $k = 9$–11 has decayed considerably due to fast Chl *b*→Chl *a* transfer, whereas the states 8 and 12, corresponding to the A_3–B_3 dimer,

remain populated much longer, although redistribution between the upper ($k = 12$) to the lower ($k = 8$) level of the dimer takes place on a sub-picosecond time scale. The picosecond dynamics of LHCII in this configuration consists mainly of slow transfer from the $k = 8$ level to the Chl *a* manifold. The Chl *a* dynamics are characterized by very fast equilibration: after 1 ps the distribution of relative populations of the $k = 1$–7 states remains virtually unchanged, only the total population of the Chl *a* band increases due to relaxation from the $k = 8$ state.

In Figure 10, the effect of direct, selective excitation of the $k = 7$ state near 660–665 nm is shown. For both the *abab* and *baab* configurations (top left and right), we observe only fast dynamics after excitation of this state, which is in contradiction with earlier pump–probe studies.[16,18] We will return to this discrepancy and the implications for the LHCII structure in the Discussion section. For the *bbaa* and *baba* configurations (bottom left and right), the Chl *a* band equilibration has a slow component, consisting of population decay from the $k = 7$ state, which is localized on the blue-shifted $B_3(a)$ site. This slow component is most pronounced upon selective excitation of the $k = 7$ state (Figure 10), but an indication of it can already be seen in Figure 9 (bottom left and right).

Excitation Dynamics in the Site Representation. The study of equilibration among the exciton states does not give us all the information about the LHCII dynamics which can be obtained from our model. After excitation by a broad pulse, a superposition of several states is populated, which gives rise to wave packet formation. Initially, this wave packet can be significantly delocalized, but after the decay of the coherences between one-exciton states, its delocalization degree will always be less than that of the individual exciton states, which we described above (see the participation ratio shown in Figure 5). Moreover, because of the wave packet dynamics, the degree of delocalization will be time dependent, with the excitation becoming progressively more localized. To study this phenomenon, we calculated the one-exciton density matrix, including the coherences between the exciton eigenstates, and transformed it back to the site representation, for several delay times. The degree of delocalization of the wave packet at a particular delay time is given by the inverse participation ratio N_ρ of this density matrix at that time.[43] Figure 11 shows the evolution of the density matrix in the site representation (averaged over disorder) for broadband Chl *b* excitation of LHCII at room temperature. This example was calculated for the *bbaa* configuration.

At the very first moment, in the leading edge of the pulse, impulsive excitation creates a nonstationary polarization which involves all spectral components of the complex. This will only survive prior to dephasing of the ground-to one-exciton coherences, for which the time scale is determined by the width of the entire LHCII absorption spectrum. Indeed, we initially observe an almost uniform, coherent excitation of the whole antenna (see the panel for $T = 0$ fs). Subsequently, the polarization approaches a stationary limit, and the pulse starts to feel the overlap between its spectrum and the absorption spectrum. From this point (see the panels for delays 20 and 40 fs) only those components grow in amplitude that are in resonance with the pump. As a consequence, we see an 8-fold increase of the population of the Chl *b* sites from 0 to 40 fs, whereas the uniform component created at zero delay remains constant and small. Thus, the amplitude of the A_1 population is about 2 (in arbitrary units) at 0, 20, and 40 fs, whereas the corresponding $A_3(b)$ populations are 2, 8, and 16. The switch from uniform to more selective excitation during the interaction between antenna and pump pulse is accompanied by a decrease
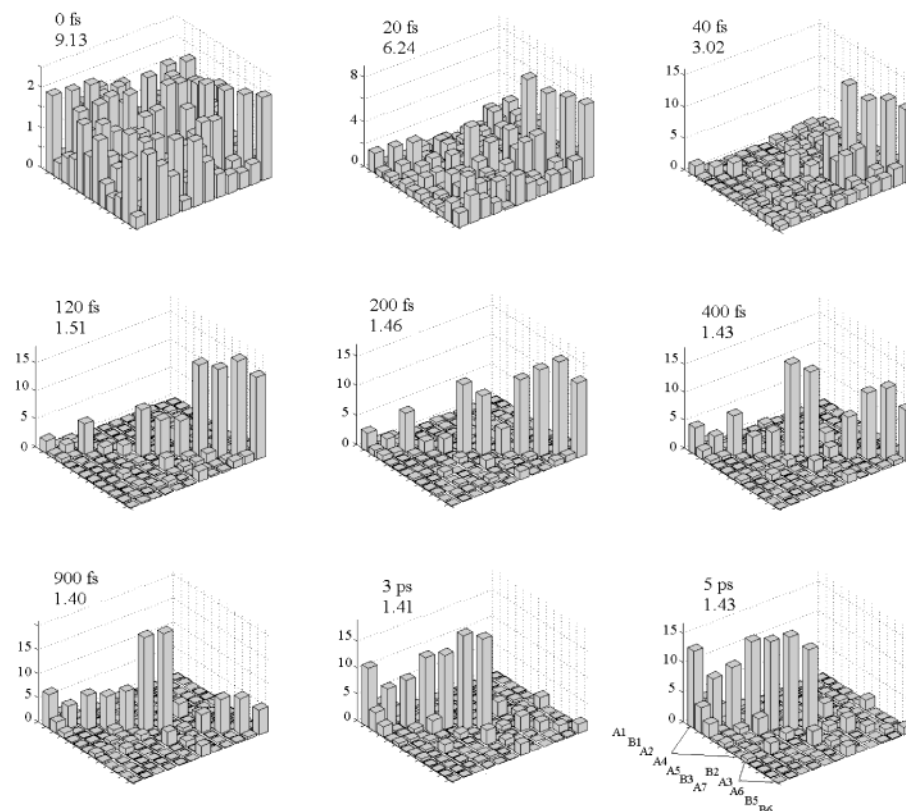
LHCII Complex of Higher Plants

J. Phys. Chem. B, Vol. 107, No. 8, 2003 **1905**

Figure 11. Evolution of the one-exciton density matrix (in the site representation) upon blue side excitation (645 nm) with the 70 fs laser pulse. The absolute values of the density matrix (averaged over disorder) are shown. The *bbaa* configuration is used in this example. Time delays are 0, 20, 40, 120, 200, 400, 900, 3000, and 5000 fs as counted from the maximum of the excitation pulse. The numbers below the time delay values show the corresponding delocalization size of the exciton wave packet determined as the inverse participation ratio of the density matrix. Note that we use a special order of the sites to highlight the transfer from *b* to *a* sites (as shown in the 5 ps panel). The density matrix amplitudes are shown in the same units for all delays (note a different scales for the first three panels).

in the delocalization value from 9 to 3. The coherence between the resonant Chl *b* sites, seen from the relative amplitudes of the off-diagonal elements in the Chl *b* region, is almost the same from 0 to 40 fs delay. From 40 to 120 fs, when the antenna is no longer interacting with the pump, these coherences decay rapidly, leading to the formation of an almost localized (diagonal) density matrix in the Chl *b* region. The total inverse participation ratio drops from 3 to 1.5 during this time interval.

The period after 120 fs is characterized by population dynamics. In the sub-picosecond range, this consists of transfer from the Chl *b* to the Chl *a* sites, in this configuration predominantly to the localized B_3 and A_7 sites. Some direct Chl *b*→Chl *a* transfer to the A_1−B_1−A_2 and A_4−A_5 clusters also takes place. As described previously, the exciton states of these clusters are delocalized and the intracluster dynamics are characterized by sub-picosecond equilibration of the exciton state populations. Subsequent ps dynamics of the complex mainly consist of the redistribution of excitation density between the Chl *a* sites B_3 and A_7, and the remaining five quasi-equilibrated Chl *a* sites. In the steady-state limit, the excitation tends to reside on the A_1−A_2−B_1 and A_4−A_5 clusters, which are the main contributors to the lowest exciton states of the LHCII antenna.

Discussion and Conclusion

In this section, we will discuss some implications of our results for the LHCII antenna. Our results will be compared with previous calculations of LHCII properties. We will first discuss the steady-state (structural) characteristics of LHCII, and then the energy-transfer dynamics.

LHCII Structure and Steady-State Properties. *Site Identities*. On the basis of our modeling, we have proposed four different configurations of binding site identities. For each of them, a good match with nearly all LHCII properties was obtained, suggesting that all LHCII complexes could be in one of these configurations. Of course, such fixed site identities would not agree with biochemical studies on mutant monomeric LHCIIs. Moreover, note that we are selective for configurations with the standard stoichiometry of seven Chls *a* and five Chls *b*, since others will not provide a good match for the absorption spectrum. Thus, the possibility that a fraction of LHCIIs could have a different stoichiometry with a different mixed site occupancy is neither ruled out nor confirmed.

Looking at the proposed configurations more specifically, we discern small discrepancies with previous findings for each of them. In three of the four configurations, *baab*, *bbaa*, and *baba*, a Chl *b* is bound to site A_3. Although this site was found to have a mixed Chl *b*:Chl *a* affinity,[4,6] a full Chl *b* character for this site can be ruled out on the basis of the mutant-minus-wild-type absorption difference spectrum, which peaks at 662 nm,[4,5] and of the large amount of Chl *a* loss in these mutants.[4−6] The fourth configuration, *abab*, is also in conflict with biochemical work, as it was suggested [Bassi, private communication] that site A_7 always binds a Chl *b*. As it happens, our results do not confirm this proposal as we find only one configuration with this identity for A_7, *baba*, which is not a unique solution as a Chl *b* binds at site A_3. Most likely, site A_7 can bind a Chl *a* sometimes. At the same time, it seems unlikely that it would always bind a Chl *a* as would be the case if all LHCIIs were in the *abab* configuration. Nevertheless, this configuration was

previously proposed by van Amerongen and van Grondelle,[2] who found that calculations based on it fit both steady-state and dynamic properties very well.

An important consequence of the finding that none of the four configurations can be a unique solution, is the confirmation that mixed binding sites are present in the native LHCII complex, as proposed by Salverda et al.[24] The resulting mixture of LHCII complexes in these four configurations would be in very good agreement with previous suggestions for the LHCII structure. They do not deviate strongly from the original Kühlbrandt assignment[3] or from later adjustments to this assignment proposed by Kühlbrandt and co-workers.[5,7] Our calculations suggest that all four mixed sites proposed by Bassi and co-workers[4] indeed bind both Chls *a* and Chls *b*. Altogether, we propose on the basis of our modeling that a substantial fraction of LHCII complexes will be found in one of our four configurations.

Dipole Moments. For each of the four proposed configurations, the dipole moment orientations are adjusted independently. Nevertheless, these orientations turn out to be remarkably well-conserved. For three of the four configurations, the combination is exactly the same, with all the Q_y dipole moments oriented along the N_A-N_C axis (direction "0") except for that of B_3. The latter is always found to lie along N_B-N_D, regardless of its Chl *a/b* identity. This orientation for B_3 was also proposed by all other authors who calculated the LD spectrum,[2,10,11,18] and for the corresponding site in CP29 (see Gradinaru et al.[44] and references therein, İşeri et al.[45]). Most of the other dipole moments are equally well determined. Between our four configurations, only in the *bbaa* configuration two orientations are different, with the dipoles of B_5 and A_3 along the N_B-N_D axis. Note that both Chl *a* and Chl *b* can bind to site A_3 in orientation 0 according to our calculations, and that none of the dipole orientations is correlated with site identity.

For the *abab* configuration, van Amerongen and van Grondelle[2] find exactly the same combination as we do with all dipoles except that of B_3 oriented along N_A-N_C. There are a few minor differences between our results and those of İşeri and Gülen.[10] They find that the Q_y dipole moments of the Chls at A_2, A_6, and B_5 also lie along the N_B-N_D axis together with that of B_3. Furthermore, they propose a rotation of the Chl *b* dipole moments by up to 10 degrees in order to obtain a better match with the experimental LD spectrum. However, İşeri and Gülen limit themselves severely in their calculations by imposing the same dipole combination on all the 16 configurations they consider and looking only at the average of all 16 spectra. When the spectrum is optimized for a single configuration, such a rotation is probably not necessary.

Note that in view of the discrepancy between experimental and calculated LD amplitudes, the actual orientations will not be exactly equal to the 0 or 1 directions used here. Nevertheless, using the Kühlbrandt model, we propose that the dipole moments of A_1, A_4, A_5, A_7, B_1, B_2, B_3, and B_6 lie along the directions we have found, that is, all along N_A-N_C except B_3. The directions of the A_2, A_3, A_6, and B_5 dipole moments cannot be determined with certainty.

Energies. At first sight, the monomeric site energy values we need for our calculations vary significantly from one configuration to the next. Nevertheless, some clear trends can be identified. In the first place, the Chl *b* energies are all very similar, lying between 15400 and 15450 cm^{-1} in all four configurations, except for two values. Within this narrow range, the energy of each site varies randomly between different configurations. Obviously, the Chl *b* energies are not very

critical for the LHCII properties. For the Chls *a*, this is rather different. In all four configurations, A_4 is the lowest energy site. Both sites A_1 and A_2 also have low energies. Although these "red" Chls *a* pigments are strongly coupled to the more "blue" Chls *a* at sites A_5 and B_1, it is clear that these two groups will always be the low-energy sinks in the LHCII complex (see also the description of Figure 6 in the Results section). This property is remarkably robust: even for a realization of the disorder with relatively high energies for these pigments (see Table 2, with k = 4-6 states having a large $A_1-A_2-B_1$ and/or A_4-A_5 contribution), the lowest state is still localized on these pigments due to the large exciton splitting in these strongly coupled groups.

The assignment of low energies to the stromal side pigments agrees well with biochemical studies,[4,5,7] in which mutant LHCII complexes without A_1, A_2, or B_1 are found to lack oscillator strength at the red edge of the absorption spectrum, and mutants without A_4 or A_5 lack a transition at 674 nm.[4,7] On the basis of steady-state spectrum calculations, van Amerongen and van Grondelle[2] determine the same two lowest-energy sites as we do, A_4 and A_2. Furthermore, they also propose a somewhat higher energy for the Chl *a* at A_5, to explain the slow decay of blue Chl *a* absorption observed in experimental kinetics.[16-19,22] This high energy for A_5 would also be in agreement with the observed lack of intratrimer transfer, for which this site is the main bridgehead together with A_4, at low temperature.[45] With regards to the stromal side pigments, the only disagreement with literature is found when we compare our results to those of İşeri and Gülen,[10] who propose very high energies for A_2 and B_1, an unlikely assignment in view of the biochemical results[4,5,7] (and their functional role, see below).

We find that the bluemost Chls *a* nearly always lie on sites A_3 or B_3 except in configuration *abab* where B_1 occupies the blue end of the spectrum. The location of isolated Chls *a* on the lumenal side of the membrane agrees with the finding that relaxation is slow when blue Chls *a* are excited. Very blue Chl *a* absorption, around 662 nm, was also found for A_3 and B_3 with site-selective mutagenesis studies.[4,5,7]

We find that the transitions of the remaining Chls *a* on sites A_6 and/or A_7 lie somewhere in the middle. This is not completely in agreement with the results of van Amerongen and van Grondelle,[2] who propose that A_7 is the bluemost Chl *a* in the *abab* configuration rather than B_1. Nevertheless, the same overall picture emerges from the literature and from our results: Chl *a* excited-state population will flow from high-energy exciton states on the lumen side of LHCII to low-energy states on the stromal side. This picture agrees very well with the functional role of the A_4-A_5 and $A_1-A_2-B_1$ groups, which probably serve as contact points with other monomers within the trimer and as the connection to other trimers.[2,3] At low temperature, time-dependent localization of the exciton wave packet will occur within the stromal side groups on one of the lowest-state pigments, A_4 or A_2.

LHCII Dynamics. *Energy Transfer Rate Attributions.* Although the importance of exciton interaction for the description of LHCII has been widely recognized, so far excitonic models were only used to calculate steady-state properties. Calculations of energy-transfer dynamics have thus far always been carried out on the basis of Förster theory, with the implicit assumption that all states are fully localized.[2,10,18,46] Renger et al.[27] used the Redfield theory, but their analysis was restricted to the dynamics within a Chl *b*−Chl *a* heterodimer. The work described in this paper is the first attempt to include the energy transfer properties of the whole LHCII antenna in an excitonic picture. To enable a comparison with previous calculations, we

LHCII Complex of Higher Plants

J. Phys. Chem. B, Vol. 107, No. 8, 2003 **1907**

will first make a few general remarks about the meaning of various transfer rates which are mentioned in this paper and in the literature.

In the first place, in our simulations each pair of excitonic eigenstates is connected with an individual relaxation rate. An example of these $N^2 = 144$ rates for a particular choice of configuration and disorder was given in Table 2. They are relatively fast: almost all 12 exciton states are connected to at least one other state with a subpicosecond pairwise rate. Some partial sums of these rates, such as from one single "Chl b" state ($k = 8-12$) to all of the "Chl a" states ($k = 1-7$) were also specified in Table 2. Second, there are $N = 12$ kinetic components given by eigenvalues K_{ET} of the relaxation tensor, i.e., $\det|K_{ET} - R_{k'k'kk}| = 0$. These components (which are different from pairwise rates) determine the overall excitation dynamics. They correspond to the decay rates that are usually extracted from experimental kinetics. Thus, experimental papers on kinetic measurements with techniques such as pump−probe, fluorescence, 3PEPS, or two-photon echo (2PE)[15−24,47,48] identify a (small) number of decay time constants, derived by fitting a multiexponential decay function to the experimental data. For example, an exponential fitting of experimental TA kinetics,[22] revealed components of 175 fs (40% amplitude), 625 fs (40%), and 5 ps (20%), together with an almost constant component of >790 ps. For comparison, our model (for the realization shown in Table 2) gave $K_{ET}^{-1} = 0.116, 0.138, 0.171, 0.203, 0.223, 0.283, 0.421, 0.522, 0.616, 1.124, 3.342,$ and 231.6 ps. Thus, we have five components of 120−220 fs, 4 components of about 300−600 fs, 1.1 and a 3.3 ps components, and a long (almost constant) component. We cannot estimate the amplitudes of these components (which are dependent on excitation conditions), because we did not make a deconvolution of the calculated kinetics. After averaging over the disorder, we still obtain values in the same range. Altogether, the correspondence between our results and these and other experimental values is quite good, except for the slowest rates, a fact which we will discuss in more detail below.

Third, in several previous papers about energy transfer in LHCII,[2,10,16,18,46] transfer rates between specific pairs of Chl sites are calculated using Förster theory. Clearly, these rates will be significantly different from the relaxation/hopping rates between delocalized exciton states obtained within the limits of Redfield approach. On the other hand both Förster and Redfield pairwise rates cannot be directly compared with the overall kinetic components extracted from experiment. However, these comparisons work reasonably well thanks to the fact that the main concern of most authors lies in the identification of Chl b→Chl a transfer rates. The experimental kinetics observed with transient absorption is to a large part determined by the shift of excitation due to this transfer. Also, the exciton states involved are virtually localized on either Chls b or Chls a. Below, we will see that as a consequence the values for Chl b→Chl a transfer are not very different between our simulations, experiments and Förster-based calculations. Nevertheless, the difference between the approaches becomes clear for isoenergetic energy transfer. On the bases of the parameters derived for Chl b→Chl a transfer, several authors[2,10,18] have also calculated pairwise rates for steps between Chls b and between Chls a using the Förster equation. Those rates do not correspond as well to our results as will become clear below.

Chl b to Chl b Transfer. In three of the four configurations we consider, namely, *abab*, *bbaa*, and *baba*, the five Chl b states of the LHCII complex fall into the following pattern. Three states are almost localized on a particular Chl b site and the

other two states are delocalized over a dimer. The dimer is found in the $A_6−A_7−B_5−B_6$ compartment, with the specific Chls involved depending on the configuration and the disorder. For the example in Table 2 we find a 60%/40% mixing of the A_6 and B_6 single-site excitations. For this type of Chl b state distribution, subpicosecond relaxation takes place within the dimer whereas the pairwise rate between any of the near-localized states and the other four Chl b states is at most 0.5 ps^{-1}. Only for the fourth configuration, *baab*, we calculate that, for most realizations of the disorder, two dimers with subpico-second relaxation are present, with the most strongly coupled one localized on the $A_3−B_3$ sites.

Delocalization between Chl b sites was not explicitly considered by other authors when they calculated energy transfer rates. Van Amerongen and van Grondelle[2] find only picosecond transfer times when they apply the Förster equation to the *abab* configuration. For the $A_6−B_6$ pair they calculate a rate of 0.36 ps^{-1}. İşeri and Gülen[10] do find delocalized Chl b exciton states, but for calculating transfer times they recur to the Förster equation. Nevertheless, they find a rate similar to ours for the $A_6−B_6$ pair of (300 fs)$^{-1}$. It is rather surprising that their rate is so different from that of van Amerongen and van Grondelle[2] for this particular pair, as most of their rates are much more similar. Gradinaru et al.[18] calculate a 3 ps transfer time between Chls b at sites A_6 and B_6. Altogether, we conclude that the coupling strength within this dimer and similar dimers in the $A_6−A_7−B_5−B_6$ compartment leads to considerable delocalization and the Förster approach should not be applied.

The existence of a Chl b dimer was first suggested by Agarwal et al.[23] To explain the fast decay observed in their 650 nm 3PEPS measurements, Agarwal et al. as well as Salverda et al. conclude that at least two fast-transferring Chls b are present in some of the LHCII complexes. Agarwal et al. propose a dimer which was incorrectly based on the assignment of Gradinaru et al.,[18] consisting of a Chl b at site A_5 (which they renamed B_6) and a Chl b at site B_5. For this dimer they calculate a transfer time using the Förster equation, which yields a value of 1300 fs, rather slower than the 3PEPS decay times of 300 and 800 fs they find. Nevertheless, in this hypothetical config-uration the corresponding exciton states would be delocalized over these two sites and the exciton relaxation rate would be much faster than the Förster value of (1300 fs)$^{-1}$, analogous to the difference between our rate and the rate of van Amerongen and van Grondelle[2] for the $A_6−B_6$ dimer.

Assuming a direct correspondence between the 3PEPS decay rate of 150 fs which they observe and a pairwise Chl b−Chl b transfer rate, taken from the Förster-based calculations of İşeri and Gülen,[10] Salverda et al.[24] propose that the $A_3−B_3$ dimer should be responsible for this decay. From this, it follows that this pair should be a Chl b dimer in some of the complexes, in line with mixed site occupancy. However, we obtain a good match for the 650 nm peak shift decay in three other configura-tions with more weakly coupled Chl b dimers. At this point, we recall that this may well only work because Chl b→Chl a transfer strongly influences our calculated 3PEPS decay at 650 nm. There are at least three reasons for such a strong influence. In the first place, the transfer between the Chl b states is strongly influenced by Chl b→Chl a transfer because of the nonuniform connections of these states to the Chl a states, which will perturb the equilibrium between the Chl b state populations. However, this explanation brings us to a problem with energy transfer between localized Chl b states. For Chl b states which are over 90% localized on a single Chl b, such as $k = 8$ in Table 2, one would expect that the correspondence between a pairwise

relaxation rate and a site-to-site rate based on Förster theory would be better than for delocalized dimers. Rather, it turns out that the opposite is true, with a factor of 10 difference between our rates and the slow rates that van Amerongen and van Grondelle[2] find for Chl *b*−Chl *b* transfer. It is not likely that Förster is at fault here, because that should give a good approximation for both 90% and 99% localization, whereas our method would give a factor of 10 difference between these cases. An adequate description should also take into account that the 90% localized state will become completely localized due to thermal fluctuations. What the effect of this would be on a simulation of the 650 nm peak shift decay cannot be concluded from our calculations.

Second, the change in ratio of Chl *b* state populations induced by *b*→*a* transfers can change the rephasing capability, and thus the peak shift, even in the absence of any intraband *b*→*b* transfer. At first glance, it seems that transfer out of the laser window cannot contribute to the dephasing, but this is true only for isoenergetic *b* states. A finite splitting introduces an additional inhomogeneity next to the inhomogeneous broadening of the individual *b* states. If some of the *b* states can no longer contribute due to transfer out of the band, the effective inhomogeneity of the Chl *b* ensemble will be changed, thus affecting the peak shift prior to transfer between *b* states. We have checked this for a dimeric model system (not shown). Unfortunately, the quantitative effect of this dephasing mechanism could not be checked. Thus, whether the 650 nm peak shift decay can still be reproduced in the absence of any Chl *b* intraband transfer cannot be said.

Third, a significant contribution of Chl *a* to the peak shift can be explained by supposing that the highest Chl *a* states are directly excited by our spectrally wide pulse. In two of our configurations, for example, the $k = 7$ state is largely localized on the B_3 (Chl *a*) site, and fast $A_3 \rightarrow B_3$ transfer makes an important contribution to the 650 nm peak shift decay, just like when a Chl *b* pair is present at these sites.

Summarizing our findings, we conclude that sub-picosecond Chl *b*→Chl *b* transfer does occur in LHCII. However, this transfer probably does not dominate the 650 nm peak shift decay as much as was previously thought.[23,24] In line with previous calculations,[2,10,18,46] the main pathway of excitation flow is from Chl *b* to Chl *a* directly.

Chl b to Chl a Transfer. Three of the configurations (*abab*, *bbaa*, and *baba*) contain a Chl *b* dimer and 3 near-localized Chl *b* states. In these configurations, all Chls *b* are relatively close to Chls *a*, and nearly all Chl *b* to Chl *a* transfer takes place on a subpicosecond time scale. As a typical example, the summed rates given in Table 2 for transfer from each Chl *b* state to all Chl *a* states taken together, have values of 6.4, 4.0, 1.8, 1.4, and 0.6 ps^{-1}. This amplitude distribution, of 40% for a 160−250 fs component, 40% for a 550−720 fs component, and 20% for slower (1.7 ps) transfer, is close to the distribution of the overall kinetic components K_{ET}^{-1} (120−220 fs, 300−600 fs, and 1.1 and 3.3 ps as mentioned above) and also corresponds well to the experimental transient absorption decay components at room temperature. As said above, this is to be expected as the overall kinetics correspond to a large extent to the major excitation shift in the LHCII complex, which is from Chl *b* to Chl *a*. Förster-theory based calculations[2,10,16,18,46] invariably yield similar values for configurations such as the three in question.

A less good agreement is found for the slow part of the Chl *b* to Chl *a* transfer with these three configurations. Especially for configurations *abab* and *baba*, the slow part of the

experimental TA kinetics is not very well reproduced. When we compare the rates, the slow transfer we find is always too fast, with $K_{ET}^{-1} = 3$ ps rather than 4−9 ps for the longest lived Chl *b* state. On the other hand, the fourth configuration, *baab*, shows a good match for the slow part of the TA kinetics, due to very slow relaxation from the Chl *b* dimer on $A_3−B_3$ to any of the Chl *a* states. However, the corresponding amplitude distribution of 20% sub-picosecond and 80% picosecond lifetimes for the Chl *b* states is definitely not in agreement with previous findings. Most likely, the solution for this discrepancy is similar to that for the Chl *b*→Chl *b* transfer. The fast processes are well described by our modeling, and the slowest rate should be calculated in the localized limit using the Förster equation. Altogether, we conclude that the distribution of rates for Chl *b* to Chl *a* transfer is well established for the LHCII complex and the values are close to the calculated K_{ET} values and to the pairwise rates, except for the slowest rate which will be about 5 ps.

Chl a to Chl a Transfer. With respect to the Chl *a* excitation dynamics, two different patterns are found in our simulations. For two configurations, *baab* and *abab*, all Chl *a* excitation ends up in the lowest two or three states within a few 100 fs. This is not in agreement with experimental TA kinetics, which show that at 662 nm, bleaching persists for at least 2.5 ps.[16,18] Previous calculations have reproduced this slow lifetime by proposing a localized highest Chl *a* state either in the $A_6−A_7−B_6−B_5$ compartment (A_7 in ref 2) or in the $A_3−B_3$ pair (ref 18). For the other two configurations, *bbaa* and *baba*, we do reproduce this slow transfer component, as the highest Chl *a* exciton state ($k = 7$) is mainly localized on site B_3 and lives for several picoseconds. Unfortunately, we did not have an experimental 662 nm pump−probe decay trace for direct comparison to our modeling. Nevertheless, we expect that the decay of our modeled curve would be too fast for the *baab* and *abab* configurations and close to experiment for the *bbaa* and *baba* configurations.

For all four configurations, we calculate that the intermediate states which absorb around 670 nm live only for a few 100 fs (see, e.g., Table 2 and Figure 10). This appears to be in contradiction with experimental TA kinetics at room temperature, as a <300 fs and a 6 ps component were observed with about equal amplitudes for 670 nm bleaching.[16−19,22] For a better comparison, we have separately calculated the seven eigenvalues K_{ET} of the Chl *a*−Chl *a* relaxation tensor for the realization shown in Table 2 and we find time constants of 0.119, 0.225, 0.287, 0.520, 0.618, 6.24, and an almost constant value. Thus, besides the fast components of 120−280 and 500−600 fs, we also obtain a 6 ps component. This component is as slow as the experimental one, but it is not clear how big its amplitude is (it should be about 50% for Chl *a*→Chl *a* transfer). An indication that slow kinetics is correctly reproduced in Chl *a* equilibration can be seen from the simulated 670 nm 3PEPS decay, for which the match to the experimental curve is rather good for all four configurations. Note that transfer times in the range of 10 ps were calculated using the Förster equation by van Amerongen and van Grondelle,[2] and by İşeri and Gülen,[10] for transfer from isolated Chls *a* on the lumen side (e.g., A_3) supposed to absorb at 670 nm or more to the blue, to the groups (e.g., $A_1−A_2−B_1$) at the stromal side, supposed to absorb at 675 nm or at longer wavelengths.

Despite the good match between our simulation and the experimental curve, our interpretation of the 670 nm 3PEPS is not the same as that of Salverda et al.[24] As mentioned before, almost all excitation flows to the lowest 2 or 3 Chl *a* states, which reside on the $A_1−A_2−B_1$ and/or $A_4−A_5$ groups, within

a few 100 fs according to our modeling, except for a long-lived state on B_3. Together with the coherent artifact, these fast dynamics explain the large 3PEPS decay within 200 fs. However, our match with the 670 nm transient grating is not so good and this is probably due to the fact that the lowest 1 or 2 states are not within reach of the laser pulse. Arguing that this is indeed the case, Salverda et al. suggest that the chlorophylls at the stromal side would absorb too much to the red to contribute much. They propose that a relatively blue-shifted Chl *a* dimer on sites A_3 and B_3 is needed to explain the fast component. We have not considered such configurations with an A_3-B_3 Chl *a* dimer in detail, as they do not yield good overall results (note that this does not exclude the presence of this dimer in some of the complexes). However, we expect that the lowest states will contribute to 3PEPS despite their less good overlap with the laser pulse, analogous to our observation that Chl *a* states contribute to the 650 nm 3PEPS. This is also indicated by the fact that for a preliminary calculation with redshifted site energies, the 3PEPS is hardly affected. Also, although the lowest states of the strongly coupled groups at the stromal side are usually the lowest states of the whole antenna complex, they can be higher in energy for some realizations of the disorder (see, e.g., Table 2 where $k = 5$ and 6 have a strong A_2-B_2 character). Altogether, we expect that relaxation within the stromal groups certainly contributes to the 670 nm peak shift decay. This finding seems to agree better with the interpretation of Agarwal et al.,[23] who simulate their 3PEPS decay with time constants taken from pump–probe kinetics, which correspond mainly to the relaxation to the lowest Chl *a* states. They do not propose any particular sites which should be involved. Note that they also observe a large sub-picosecond decay of the 670 nm TG just like Salverda et al., for which they do not offer an explanation.

Altogether, we conclude that the fast relaxation components we find are a good description of the dynamics within strongly coupled Chl *a* groups such as $A_1-A_2-B_1$ and A_4-A_5. We also observe slower Chl *a* dynamics within the complex, corresponding to transfer between monomeric (localized) states, and we find even more slow kinetic components that appear to be due to the combined action of many equilibration pathways and cannot be ascribed to any particular pairwise transfer.

Advances and Limitations of the Redfield Model. *Förster, Redfield, and Modified Redfield Approaches.* There are several different approaches to the description of energy transfer in molecular aggregates (frequently applied to photosynthetic complexes), corresponding to different physical limits. The Förster theory,[28] corresponding to the migration of localized excitations, implies a weak exciton (pigment–pigment) coupling, but it can be applied for both weak and strong electron–phonon coupling. The Redfield theory[26] describes the relaxation/migration of excitations with an arbitrary degree of delocalization (thus implying arbitrarily strong pigment–pigment interactions), but it requires a weak electron–phonon coupling. Both diagonal and off-diagonal phonon coupling are treated as a perturbation, and only single-phonon transitions are allowed. Thus, the transfer between two exciton states with a large energy gap requires the coupling to a high-frequency phonon mode. Recently, Zhang et al.[49] developed a theory where the diagonal electron–phonon coupling is treated nonperturbatively. As a result, the line shapes include strong-coupling features, like vibrational progressions and the Stokes' shift of the fluorescence (depending on the exciton state). The off-diagonal part is treated as a perturbation that induces transitions between exciton eigenstates. This theory (referred to as "modified Redfield")

was compared with the conventional Förster and Redfield approaches by Yang and Fleming,[50] who found that the modified Redfield equation includes the Förster and Redfield equations as limiting cases.

Numerical comparison of the three models (using the same phonon spectral density) shows that in the case of relatively weakly coupled pigments (20 cm^{-1} coupling strength) with a small (0–100 cm^{-1}) energy gap, the Redfield rates can be up to 10–100 times larger than the Förster rates (see Figure 2b in ref 50). This situation roughly corresponds to the above-described intraband Chl *b*–Chl *b* and Chl *a*–Chl *a* transfers involving monomeric states. On the other hand, for a larger energy gap between monomers (200–1000 cm^{-1}), the Redfield equation always gives significantly slower rates than the Förster equation (for any value of the intermolecular coupling: see the two examples in Figure 2a,b in ref 50). This range corresponds to the interband Chl *b*–Chl *a* transfer. In the case of a small gap, the modified Redfield method predicts the same rates as the Redfield rates (both different from the Förster rates in this case), whereas the modified Redfield rates coincide with the Förster rates at large gaps, when the Redfield rates are too slow. An increase in phonon density at higher frequencies gives faster Redield transfer rates for a big energy gap, but these are still slower than those obtained with the modified Redfield approach (Figure 3 in ref 50).

It was concluded by Yang and Fleming that the Redfield theory only works well for a small energy gap between the interacting states. In this case, the validity of the theory is guaranteed not by a weak coupling to the bath, but by a wide spectrum of phonons. On the other hand, a large energy gap corresponds to the Förster regime. Both these limits are covered by the modified Redfield approach, but the curves corresponding to the conventional Redfield and Förster rates are different everywhere except at their crossing point.[50] The relation between Förster and Redfield equations was also studied in ref 51.

The Spectral Density Choice. The above-mentioned examples show how sensitive the Redfield method is to the choice of the spectral density. To model the intra- and interband transfers we therefore used a spectral density with the possibility of independent variation of the positions and amplitudes of the low- and high-frequency peaks (eq A11). Below, we will compare these parameters (adjusted from the fit) with the experimental spectral density.

First of all, it should be noted that there are two different definitions of the spectral density. The experimental spectral density is usually defined as the phonon function obtained from the low-temperature fluorescence, see for example refs 35, 39, and 52. This phonon function must be multiplied by ω^2 when calculating the Redfield tensor.[53,54] In calculations the spectral density is typically defined as a Fourier transform of the correlation function of collective nuclear coordinates.[31,32,38,55] This spectral density already contains this ω^2 factor, and increases at higher frequencies,[38] in contrast to the phonon function. Our value $J_{kk'}$ is related to the latter kind of spectral density. If we compare our spectral density with the Brownian oscillator model,[55] then our couplings V_j will be related to $S_j\omega_j^2/\gamma_j$ for the low- and high-frequency peaks, where S_j are the Huang–Rhys factors, ω_j the maximum frequencies, and γ_j the damping constants. For the *bbaa* model, for example, our spectral density for the Chls *a* can be approximated by a broad high-frequency peak with $S = 0.17$ and a low-frequency peak with $S = 0.28$. The scaling factors ν_A and ν_B reflect the difference in Huang–Rhys factors S for Chls *a* and *b*. Note that our spectral density increases with the frequency gap (Table

1), in a similar way as the spectral density obtained by molecular dynamics calculations for the B850 LH2 band,[38] and as the phonon function measured for the Chl *a* band of LHCII,[39] if we multiply that by ω^2.

We also compared our spectral density quantitatively with the experimental one for LHCII (calculated from the data of Peterman et al.,[39] with the ω^2 factor included). Although the shape of the measured phonon profile is different from our model shape, we can roughly compare the two by looking at the amplitude of the low-frequency peak and the amplitude of the high-frequency maximum near 500 cm^{-1}, the frequency that corresponds to the Chl *a*−Chl *b* energy gap. We found that for the model spectral density, we need a larger amplitude at high frequencies than that seen in the experimental density profile. For example for the *abab* model, this amplitude is 1.5 times larger than in the experimental spectral density, and for the *bbaa* model it is 2.5 times larger. Such a discrepancy is probably connected with the fact mentioned above that the Redfield theory gives slower rates for a large energy gap between the states. To compensate for it, we need to increase the spectral density at high frequencies. In this respect it will be interesting to compare our results with a more realistic model (such as modified Redfield) including also a realistic experimental spectral density (work in progress).

Appendix A

Photon Echo in Molecular Aggregates. We consider an aggregate containing N exciton-coupled molecules. Electronic eigenstates of the system are weakly coupled to nuclear modes (inter- and intramolecular vibrations, phonons) that can be treated as a thermal bath inducing relaxation in a manifold of electronically excited (exciton) states. Thus, we restrict ourselves to a purely exciton dynamics, neglecting a contribution from nuclear motion to the photon echo signal.

The system Hamiltonian in the eigenstate basis is

$$H = \omega_g |g\rangle\langle g| + \sum_k \omega_k |k\rangle\langle k| + \sum_q \omega_q |q\rangle\langle q| \quad (A1)$$

where ω_g, ω_k, and ω_q are the energies of the ground (*g*) and one- and two-exciton states (*k* and *q*). The interaction with the laser field is described by

$$H_E = -\mathbf{E}(t)[\sum_k \mathbf{d}_{kg}|k\rangle\langle g| + \sum_{k,q} \mathbf{d}_{qk}|q\rangle\langle k|] + \text{h.c.}$$

$$\mathbf{E}(t) = \mathbf{E}_1(\omega_1,t) + \mathbf{E}_2(\omega_2,t) + \mathbf{E}_3(\omega_3,t) + \text{c.c.}$$

$$\mathbf{E}_1(\omega_1,t) = \mathbf{e}_1\epsilon_1(t + T + \tau)e^{-i\omega_1 t + i\mathbf{k}_1\mathbf{r}}$$

$$\mathbf{E}_2(\omega_2,t) = \mathbf{e}_2\epsilon_2(t + T)e^{-i\omega_2 t + i\mathbf{k}_2\mathbf{r}}$$

$$\mathbf{E}_3(\omega_3,t) = \mathbf{e}_3\epsilon_3(t)e^{-i\omega_3 t + i\mathbf{k}_3\mathbf{r}} \quad (A2)$$

where $\mathbf{d}_{kg}$ and $\mathbf{d}_{qk}$ are dipole moments for the $g{\rightarrow}k$ and $k{\rightarrow}q$ transitions. The external field is represented by three optical pulses with the frequencies ω_1, ω_2, ω_3, wavevectors $\mathbf{k}_1$, $\mathbf{k}_2$, $\mathbf{k}_3$,

polarization vectors $\mathbf{e}_1$, $\mathbf{e}_2$, $\mathbf{e}_3$, and envelops ϵ_1, ϵ_2, ϵ_3. The delay between first two pulses is τ, the delay between second and third interaction (population period) is T. In the case of negative τ the arguments of ϵ_1 and ϵ_2 in eq A2 must be interchanged. The population period T is always positive.

The three-pulse photon echo signal is given by[55]

$$S_{PE}(\tau,T) = \int_{-\infty}^{\infty} dt |\langle \mathbf{P}^{(3)}(\tau,T,t,\mathbf{k}_a,\omega_a)\rangle_\mathbf{e}|^2$$
$$(A3)$$

$$\mathbf{P}^{(3)}(\tau,T,t,\mathbf{k}_a,\omega_a) = e^{-i\omega_a t + i\mathbf{k}_a\mathbf{r}}\{\sum_k \mathbf{d}_{gk}\rho_{kg}^{(3)}(\omega_a) + \sum_{k,q}\mathbf{d}_{kq}\rho_{qk}^{(3)}(\omega_a)\}$$

where $\mathbf{P}^{(3)}$ denotes the nonlinear (third-order) polarization created by three interactions with the laser fields $\mathbf{E}_3$, $\mathbf{E}_2$, and $\mathbf{E}_1^*$. The angular brackets indicate the averaging over the static disorder and over orientations of the aggregate with respect to the laser field, the index $\mathbf{e}$ denotes the projection to the plane normal to $\mathbf{k}_A = \mathbf{k}_3 + \mathbf{k}_2 - \mathbf{k}_1$. The slowly varying amplitudes of the reduced density matrix $\rho_{kg}^{(3)}(\omega_a)$ and $\rho_{qk}^{(3)}(\omega_a)$ can be obtained from the Liouville equation in third order with respect to the external field:

$$\frac{d\rho}{dt} = -i[H + H_E,\rho] - R\rho \quad (A4)$$

where R is the Redfield superoperator describing the relaxation in the limit of weak coupling of the electronic coordinates to the thermal bath.

The integrated echo signal given by eq A3 is a function of τ and T. The three-pulse echo peak shift (3PEPS) is the value of τ corresponding to the maximum of the echo signal. The transient grating (TG) intensity is defined as the photon echo signal at $\tau = 0$. The thus defined 3PEPS and TG intensity are the functions of the population period T.

The Third-Order Expansion of the Density Matrix Equation. We use the following notations: $\rho_{kg}^{(n)}$, $\rho_{kk'}^{(n)}$, $\rho_{qg}^{(n)}$, and $\rho_{qk}^{(n)}$ denote the density matrix element corresponding to a coherence between the pair of states (including the ground state and the excited states from the one- and two-exciton manifold) in the nth order with respect to the external field. The $\rho_{gg}^{(n)}$ and $\rho_{kk}^{(n)}$ elements correspond to a population of the ground state and of the kth one-exciton state. Initially, i.e., before excitation $\rho_{gg}^{(0)} = 1$, whereas the nth order correction $\rho_{gg}^{(n)}$ describes a bleaching of the ground state. It is convenient to introduce a slowly varying amplitude of the matrix element oscillating with frequency ω, i.e., $\rho_{kg}^{(n)} = \rho_{kg}^{(n)}(\omega)\exp(-i\omega t)$. The transition frequencies are defined as $\omega_{kg} = \omega_k - \omega_g$ and similarly for the other pairs of states. Everywhere below we use a rotating wave approximation.

In first order the $\mathbf{E}_1^*$ or $\mathbf{E}_{2,3}$ fields create coherences between the ground and one-exciton states:

$$\left[\frac{d}{dt} + i(\omega_{kg} - \omega_{2,3})\right]\rho_{kg}^{(1)}(\omega_{2,3}) = -[R\rho^{(1)}(\omega_{2,3})]_{kg} + i\epsilon_{2,3}(\mathbf{e}_{2,3}\mathbf{d}_{kg})$$
$$(A5)$$

$$\left[\frac{d}{dt} + i(\omega_{gk} + \omega_1)\right]\rho_{gk}^{(1)}(-\omega_1) = -[R\rho^{(1)}(-\omega_1)]_{gk} - i\epsilon_1^*(\mathbf{e}_1\mathbf{d}_{gk})$$

The decay of the ground to one-exciton coherences is described by the action of the Redfield superoperator on $\rho^{(1)}$. Generally the relaxation term $R\rho^{(1)}$ is nondiagonal, thus including a coherence transfer processes.

In second order the $(\mathbf{E}_1^*\mathbf{E}_{2,3} + \mathbf{E}_{2,3}\mathbf{E}_1^*)$ interactions create an excitation in the one-exciton manifold given by a superposition

of the amplitudes $\rho_{kk'}^{(2)}(\omega_{2,3} - \omega_1)$ together with a hole in the ground state given by $\rho_{gg}^{(2)}(\omega_{2,3} - \omega_1) = \sum_k \rho_{kk}^{(2)}(\omega_{2,3} - \omega_1)$. The $(\mathbf{E}_3\mathbf{E}_2 + \mathbf{E}_2\mathbf{E}_3)$ interactions create a ground to two-exciton coherence $\rho_{qg}^{(2)}(\omega_2 + \omega_3)$:

$$\left[\frac{d}{dt} + i(\omega_{kk'} - \omega_{2,3} + \omega_1)\right]\rho_{kk'}^{(2)}(\omega_{2,3} - \omega_1) =$$
$$-[R\rho^{(2)}(\omega_{2,3} - \omega_1)]_{kk'} + i\epsilon_{2,3}(\mathbf{e}_{2,3}\mathbf{d}_{kg})\rho_{gk'}^{(1)}(-\omega_1) -$$
$$i\epsilon_1^*\rho_{kg}^{(1)}(\omega_{2,3})(\mathbf{e}_1\mathbf{d}_{gk'}) \quad (A6)$$

$$\left[\frac{d}{dt} + i(\omega_{qg} - \omega_2 - \omega_3)\right]\rho_{qg}^{(2)}(\omega_2 + \omega_3) =$$
$$-[R\rho^{(2)}(\omega_2 + \omega_3)]_{qg} + i\epsilon_3\sum_k(\mathbf{e}_3\mathbf{d}_{qk})\rho_{kg}^{(1)}(\omega_2) +$$
$$i\epsilon_2\sum_k(\mathbf{e}_2\mathbf{d}_{qk})\rho_{kg}^{(1)}(\omega_3) \quad (A7)$$

The time dependence of the second-order density matrix during the population period T is determined by the exciton relaxation/migration given by the action of the Redfield superoperator on $\rho^{(2)}$. Besides the true population dynamics, this "population" period will include (at least at early delays) the artifacts due to one- and two-exciton coherences and due to overlap of the three pulses.

In third-order we have a polarization with the frequency $\omega_a = \omega_3 + \omega_2 - \omega_1$ given by a superposition of the $\rho_{kg}^{(3)}(\omega_a)$ and $\rho_{qk}^{(3)}(\omega_a)$ coherences. Although the true echo is given by the $\mathbf{E}_3\mathbf{E}_2\mathbf{E}_1^*$ contribution, the real signal contains contributions from the polarization created by all possible nontime-ordered interactions, i.e., $\mathbf{E}_{3,2}(\mathbf{E}_1^*\mathbf{E}_{2,3} + \mathbf{E}_{2,3}\mathbf{E}_1^*)$ and $\mathbf{E}_1^*(\mathbf{E}_2\mathbf{E}_3 + \mathbf{E}_3\mathbf{E}_2)$:

$$\left[\frac{d}{dt} + i(\omega_{qk} - \omega_a)\right]\rho_{qk}^{(3)}(\omega_a) = -[R\rho^{(3)}(\omega_a)]_{qk} -$$
$$i\epsilon_1^*\rho_{qg}^{(2)}(\omega_3 + \omega_2)(\mathbf{e}_1\mathbf{d}_{gk}) + i\epsilon_2\sum_{k'}(\mathbf{e}_2\mathbf{d}_{qk'})\rho_{k'k}^{(2)}(\omega_3 - \omega_1) +$$
$$i\epsilon_3\sum_{k'}(\mathbf{e}_3\mathbf{d}_{qk'})\rho_{k'k}^{(2)}(\omega_2 - \omega_1) \quad (A8)$$

$$\left[\frac{d}{dt} + i(\omega_{kg} - \omega_a)\right]\rho_{kg}^{(3)}(\omega_a) = -[R\rho^{(3)}(\omega_a)]_{kg} +$$
$$i\epsilon_1^*\sum_q(\mathbf{e}_1\mathbf{d}_{kq})\rho_{qg}^{(2)}(\omega_3 + \omega_2) - i\epsilon_2\sum_{k'}\rho_{kk'}^{(2)}(\omega_3 - \omega_1)(\mathbf{e}_2\mathbf{d}_{k'g}) -$$
$$i\epsilon_2(\mathbf{e}_2\mathbf{d}_{kg})\sum_{k''}\rho_{k'k''}^{(2)}(\omega_3 - \omega_1) - i\epsilon_3\sum_{k'}\rho_{kk'}^{(2)}(\omega_2 - \omega_1)(\mathbf{e}_3\mathbf{d}_{k'g}) -$$
$$i\epsilon_3(\mathbf{e}_3\mathbf{d}_{kg})\sum_{k''}\rho_{k''k''}^{(2)}(\omega_2 - \omega_1) \quad (A9)$$

The Redfield Tensor. The Redfield tensor elements needed to obtain the relaxation terms in eqs A5–A9 can be calculated as[26,29]

$$R_{ijpl} = -\langle v_{lj}v_{ip}\rangle(J_{jl} + J_{ip}) + \delta_{lj}\sum_s\langle v_{is}v_{sp}\rangle J_{sp} + \delta_{ip}\sum_s\langle v_{ls}v_{sj}\rangle J_{sl} \quad (A10)$$

where indexes i, j, p, l, and s denote the eigenstates of the system (i.e., the ground state g, and the states from the one- and two-exciton manifold, k and q), and v_{ip} is the matrix element (in the eigenstate basis) of the system–bath interaction Hamiltonian, brackets indicating the averaging over the bath coordinates. The interaction Hamiltonians in the eigenstate v and site v_S representation are connected by the eigenfunction matrix $\mathbf{C}$ that

diagonalize the system Hamiltonian (eq A1), i.e., $v = \mathbf{C}^+ v_S\mathbf{C}$. The matrix element J_{ip} is the spectral density of the system–bath coupling. For example, supposing a two-component spectral density with the characteristic frequencies ω_{c1}, ω_{c2} and coupling strengths V_1, V_2, we can get it in a form:

$$J_{kk'} = 4(1 - \delta_{kk'})\frac{V_1W_1^2\exp(-W_1) + V_2W_2^2\exp(-W_2)}{1 + \exp(\omega_{kk'}/k_BT)} + \delta_{kk'}V_0$$

$$W_1 = \left|\frac{\omega_{kk'}}{\omega_{c1}}\right|; \quad W_2 = \left|\frac{\omega_{kk'}}{\omega_{c2}}\right| \quad (A11)$$

where V_0 is the pure dephasing parameter and k_BT is the temperature in the units of energy.

References and Notes

(1) Van Grondelle, R.; Dekker, J. P.; Gillbro, T.; Sundström, V. *Biochim. Biophys. Acta* **1994**, *1187*, 1.

(2) van Amerongen, H.; van Grondelle, R. *J. Phys. Chem. B.* **2001**, *105*, 604.

(3) Kühlbrandt, W.; Wang, D. N.; Fujiyoshi, Y. *Nature* **1994**, *367*, 614.

(4) Remelli, R.; Varotto, C.; Sandona, D.; Croce, R.; Bassi, R. *J. Biol. Chem.* **1999**, *274*, 33510.

(5) Rogl, H., Kühlbrandt, W. *Biochemistry* **1999**, *38*, 16214.

(6) Yang, C.; Kosemund, K.; Cornet, C.; Paulsen, H. *Biochemistry* **1999**, *38*, 16205.

(7) Rogl, H.; Schödel, R.; Lokstein, H.; Kühlbrandt, W.; Schubert, A. *Biochemistry* **2002**, *41*, 2281.

(8) Bassi, R.; Croce, R.; Cugini, D.; Sandonà, D. *Procl. Natl. Acad. Sci. U.S.A.* **1999**, *96*, 10056.

(9) Simonetto, R.; Crimi, M.; Sandona, D.; Croce, R.; Cinque, G.; Breton, J.; Bassi, R. *Biochemistry* **1999**, *38*, 12974.

(10) İşeri, E. I.; Gülen, D. *Eur. Biophys. J.* **2001**, *30*, 344.

(11) Gülen, D.; van Grondelle, R.; van Amerongen, H. *J. Phys. Chem. B* **1997**, *101*, 7256.

(12) Renger, Th.; May, V. *Phys. Rev. Lett.* **2000**, *84*, 5228.

(13) Schubert, A.; Beenken, W. J. D.; Stiel, H.; Voigt, B.; Leupold, D.; Lokstein, H. *Biophys. J.* **2002**, *82*, 1030.

(14) Palacios, M. A.; de Weerd, F. L.; Ihalainen, J. A.; van Grondelle, R.; van Amerongen, H. *J. Phys. Chem. B* **2002**, *106*, 5782.

(15) Bittner, T.; Wiederrecht, G. P.; Irrgang, K.-D.; Renger, G.; Wasielewski, M. R. *Chem. Phys.* **1995**, *194*, 311.

(16) Visser, H. M.; Kleima, F. J.; van Stokkum, I. H. M.; van Grondelle, R.; van Amerongen, H. *J. Chem. Phys.* **1996**, *210*, 297.

(17) Kleima, F. J.; Gradinaru, C. C.; Calkoen, F.; van Stokkum, I. H. M.; van Grondelle, R.; van Amerongen, H. *Biochemistry* **1997**, *36*, 15262.

(18) Gradinaru, C. C.; Özdemir, S.; Gülen, D.; van Stokkum, I. H. M.; van Grondelle, R.; van Amerongen, H. *Biophys. J.* **1998**, *75*, 3064.

(19) Gradinaru, C. C.; van Stokkum, I. H. M.; Pascal, A. A.; van Grondelle, R.; van Amerongen, H. *J. Phys. Chem. B* **2000**, *104*, 9330.

(20) Du, M.; Xie, X.; Mets, L.; Fleming, G. R. *J. Phys. Chem.* **1994**, *98*, 4736.

(21) Bittner, T.; Irrgang, K.-D.; Renger, G.; Wasielewski, M. R. *J. Phys. Chem.* **1994**, *98*, 11821.

(22) Connelly, J. P.; Müller, M. G.; Hucke, M.; Gatzen, G.; Mullineaux, C. W.; Ruban, A. V.; Horton, P.; Holzwarth, A. R. *J. Phys. Chem. B* **1997**, *101*, 1902.

(23) Agarwal, R.; Krueger, B. P.; Scholes, G. D.; Yang, M.; Yom, J.; Mets, L.; Fleming, G. R. *J. Phys. Chem. B* **2000**, *104*, 2908.

(24) Salverda, J. M.; Vengris, M.; Krueger, B. P.; Scholes, G. D.; Czarnoleski, A. R.; Novoderezkhin, V.; van Amerongen, H.; van Grondelle, R. *Biophys. J.* **2003**, *84*, 450.

(25) Yang, M.; Fleming, G. R. *J. Chem. Phys.* **1999**, *111*, 27.

(26) Redfield, A. G. *Adv. Magn. Reson.* **1965**, *1*, 1.

(27) Renger, Th.; Voigt, J.; May, V.; Kühn, O. *J. Phys. Chem.* **1996**, *100*, 15654.

(28) Förster, Th. In *Modern Quantum Chemistry*; Academic Press: New York, 1965; Vol. III, p 93.

(29) Pollard, W. T.; Felts, A. K.; Friesner, R. A. *Adv. Chem. Phys.* **1996**, *93*, 77.

(30) Kühn, O.; Sundström, V. *J. Chem. Phys.* **1997**, *107*, 4154.

(31) Chernyak, V.; Minami, T.; Mukamel, S. *J. Chem. Phys.* **2000**, *112*, 7953.

(32) Dahlbom, M.; Minami, T.; Chernyak, V.; Pullerits, T.; Sundström, V.; Mukamel, S. *J. Phys. Chem. B* **2000**, *104*, 3976.

(33) van Grondelle, R.; Novoderezhkin, V. *Biochemistry* **2001**, *40*, 15057.

(34) Novoderezhkin, V.; van Grondelle, R. *J. Phys. Chem. B* **2002**, *106*, 6025.

(35) Kühn, O.; Sundström, V.; Pullerits, T. *Chem. Phys.* **2002**, *275*, 15.

(36) Becker, M.; Nagarajan, V.; Parson, W. W. *J. Am. Chem. Soc.* **1991**, *113*, 6840.

(37) Knox, R. S. In *PS2001 Proceedings*, *12th International Congress on Photosynthesis*; CSIRO Publishing: Melbourne, Australia, 2001.

(38) Damjanović, A.; Kosztin, I.; Kleinekathöfer, U.; Schulten, K. *Phys. Rev. E* **2002**, *65*, 031919.

(39) Peterman, E. J. G.; Pullerits, T.; van Grondelle, R.; van Amerongen, H. *J. Phys. Chem. B* **1997**, *101*, 4448.

(40) Reddy, N. R. S.; Cogdell, R. J.; Zhao, L.; Small, G. J. *Photochem. Photobiol.* **1993**, *57*, 35.

(41) van Amerongen, H.; Kwa, S. L. S.; van Bolhuis, B. M.; van Grondelle, R. *Biophys. J.* **1994**, *67*, 837.

(42) Zucchelli, G.; Garlaschi, F. M.; Jennings, R. C. *Biochemistry* **1996**, *35*, 16247.

(43) Meier, T.; Chernyak, V.; Mukamel, S. *J. Phys. Chem. B* **1997**, *101*, 7332.

(44) Gradinaru, C. C.; Pascal, A. A.; van Mourik, F.; Robert, B.; Horton, P.; van Grondelle, R.; van Amerongen, H. *Biochemistry* **1998**, *37*, 1143.

(45) İşeri, E. I.; Albayrak, D.; Gülen, D. *J. Biol. Phys.* **2000**, *26*, 321.

(46) Trinkunas, G.; Connelly, J. P.; Müller, M. G.; Valkunas, L.; Holzwarth, A. R. *J. Phys. Chem. B* **1997**, *101*, 7313.

(47) Savikhin, S.; van Amerongen, H.; Kwa, S. L. S.; van Grondelle, R.; Struve, W. S. *Biophys. J.* **1994**, *66*, 1597.

(48) Hillmann, F.; Voigt, J.; Redlin, H.; Irrgang, K.-D.; Renger, G. *J. Phys. Chem. B* **2001**, *105*, 8607.

(49) Zhang, W. M.; Meier, T.; Chernyak, V.; Mukamel, S. *J. Chem. Phys.* **1998**, *108*, 7763.

(50) Yang, M.; Fleming, G. R. *Chem. Phys.* **2002**, *275*, 355.

(51) Pullerits, T. *J. Chin. Chem. Soc.* **2000**, *47*, 773.

(52) Wendling, M.; Pullerits, T.; Przyjalgowski, M. A.; Vulto, S. I. E.; Aartsma, T. J.; van Grondelle, R.; van Amerongen, H. *J. Phys. Chem. B* **2000**, *104*, 5825.

(53) Prokhorenko, V. I.; Holzwarth, A. R. *J. Phys. Chem. B* **2000**, *104*, 11563.

(54) Renger, Th.; May, V.; Kühn, O. *Phys. Rep.* **2001**, *343*, 137.

(55) Mukamel, S. *Principles of Nonlinear Optical Spectroscopy*; Oxford University Press: New York, 1995.